

Carbon and oxygen isotope microanalysis of calcite in the Permian Kupferschiefer system, Saale subbasin, eastern Germany

Mohammed S. Mohammedyasin^{a,b,*}, Joseph M. Magnall^a, Sarah A. Gleeson^{a,b}, Hans-Martin Schulz^a, Maria Rosa Scicchitano^a

^a GFZ German Research Centre for Geosciences, 14473 Potsdam, Germany

^b Institute of Geological Sciences, Freie Universität Berlin, Malteserstrasse, 74-100, Berlin 12249, Germany

ARTICLE INFO

Editor: Dr. Marco Fiorentini

Original content: [Carbon and oxygen isotope in situ analysis of calcite using secondary ion mass spectrometry in the Permian Kupferschiefer system, Saale subbasin, eastern Germany](#) ([Original data](#))

Keywords:

Calcite
Carbon isotopes
Oxygen isotopes
SIMS
Kupferschiefer
Sediment-hosted stratiform Cu (SSC) deposits

ABSTRACT

The Kupferschiefer district in Central Europe contains some of the world's highest-grade sediment-hosted stratiform Cu (SSC) deposits. In the Saale subbasin (eastern Germany), high-grade sulfides formed via replacement of calcite cement in the continental sandstones of the uppermost Rotliegend (S1), the overlying organic-rich marine mudstones of the Kupferschiefer (T1) and the Zechstein Limestone (Ca1) units. The spatial distribution of the calcite cement, therefore, had a fundamental role to play in the Cu mineralizing system. In this study, we investigate the origin of the calcite cement (and crosscutting calcite veins) using detailed petrography (cathodoluminescence, CL; scanning electron microscopy, SEM), major element chemistry (electron probe micro-analyzer, EPMA), and secondary ion mass spectrometry (SIMS) microanalyses of $\delta^{13}\text{C}$ and $\delta^{18}\text{O}$ values in drill core samples ($n = 47$) from the Saale subbasin. The calcite cement in the S1, T1 and Ca1 has a similar CL response and major element chemistry, suggestive of a common origin. Overlapping $\delta^{13}\text{C}$ and $\delta^{18}\text{O}$ values in calcite cement in samples from the S1 and T1 in the Sangerhausen and Wallendorf drill cores also suggest that the calcite cement was derived from fluids of similar composition. The low $\delta^{13}\text{C}$ values of calcite cement in samples from the S1 (-13‰ to 4.3‰ , VPDB) and T1 (-10‰ to 0.7‰) indicates carbonate alkalinity was sourced mainly from seawater-derived fluids and the oxidation of organic matter. The wide range of $\delta^{18}\text{O}$ values in the calcite cement in the S1 (-18‰ to 31‰ , VSMOW) and T1 (-22‰ to 31‰) samples suggest they are derived from pore fluids with a chemical composition influenced by early diagenetic alteration of detrital clasts, mainly dissolution of volcanic rock fragments, with minor contributions from the influx of meteoric waters and evaporated seawater. The negative $\delta^{13}\text{C}$ values (down to -15‰) in calcite veins from the T1 and Ca1 indicate sources of carbonate alkalinity derived from organic matter degradation. Our data demonstrate that no isotopic hydrothermal alteration haloes can be inferred from the $\delta^{13}\text{C}$ and $\delta^{18}\text{O}$ values in calcite cement associated with the high-grade sulfide mineralization. The lack of systematic isotopic variability in the calcite cement likely indicates the mineralizing fluid flux or temperature was not sufficient to overprint the background sources of isotopic variability, which may help to explain the modest size of SSC deposits in this part of the Kupferschiefer district.

1. Introduction

The diagenetic evolution of sedimentary rocks plays an important role in determining the petrophysical properties that control subsurface mass transfer in sedimentary basins (Bjørlykke and Jahren, 2012; Giles, 1987; Morad et al., 2000). The distribution of diagenetic carbonate often controls subsurface mass transfer, as carbonate cementation mostly occludes primary porosity but carbonate dissolution can result in the development of secondary porosity (Bjørlykke and Jahren, 2012;

Ehrenberg et al., 2012; Xiong et al., 2016; Yuan et al., 2019). Carbonate dissolution facilitates the formation of some of the largest sediment-hosted base metal deposits (Kelley et al., 2004; Pinet et al., 2022; Spinks et al., 2021; Vaughan et al., 2016; Wilkinson et al., 2015). Therefore, understanding and detecting how and where metal-bearing fluids have replaced and altered carbonate minerals is critical for effective mineral exploration in sedimentary basins (Barker and Dipple, 2019).

Sediment-hosted stratiform copper (SSC) mineralization in the

* Corresponding author at: GFZ German Research Centre for Geosciences, 14473 Potsdam, Germany.

E-mail address: moyasin@gfz-potsdam.de (M.S. Mohammedyasin).

<https://doi.org/10.1016/j.chemgeo.2023.121811>

Received 26 June 2023; Received in revised form 22 October 2023; Accepted 28 October 2023

Available online 31 October 2023

0009-2541/© 2023 The Authors. Published by Elsevier B.V. This is an open access article under the CC BY license (<http://creativecommons.org/licenses/by/4.0/>).

German and Polish Kupferschiefer districts is restricted to the southern margin of the Southern Permian Basin (SPB) (Fig. 1A; Borg et al., 2012; Mohammedyasin et al., 2023a). Here, different carbonate-bearing sedimentary units are host to Cu- and Zn–Pb sulfide mineralized rocks, which are broadly associated with a major stratigraphic redox boundary between continental sandstones of the uppermost Rotliegend

(S1) and overlying organic matter-rich mudstones of the Kupferschiefer (T1) (Fig. 1B). Sulfide mineralized rocks are also hosted by the overlying Zechstein Limestone (Ca1) and Zechstein anhydrite (A1) (Borg et al., 2012). The high-grade sulfide mineralized rocks in the Kupferschiefer district are widely associated with the epigenetic hematitic alteration known as the ‘Rote Fäule’ (Borg et al., 2012; Pieczonka et al., 2008;

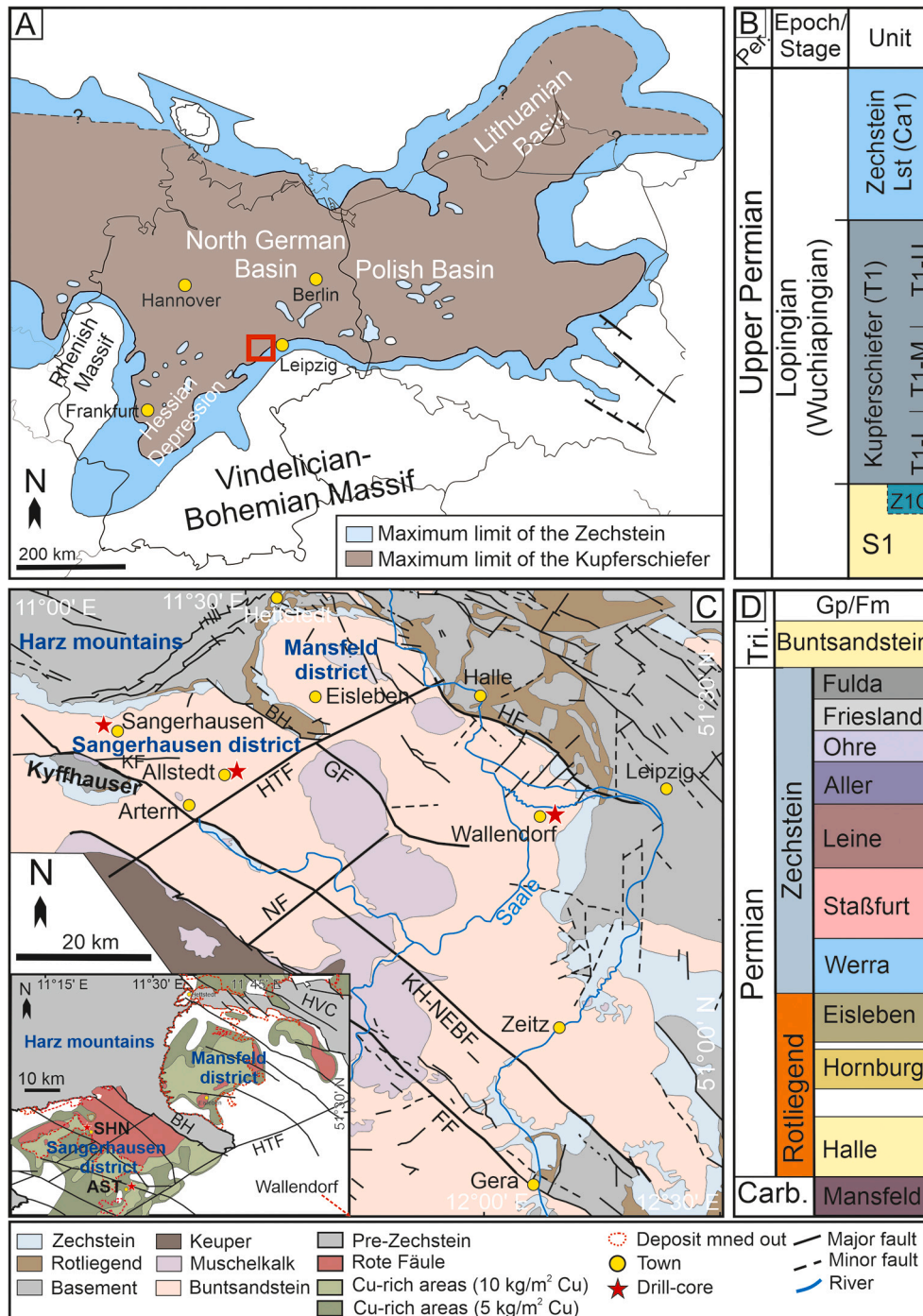


Fig. 1. (A) Simplified map showing the extent of the Zechstein and Kupferschiefer in the Southern Permian Basin (SPB) (modified after Erzberger et al., 1968; Kulick et al., 1984; Paul, 2006). The red square shows the approximate location of the Saale subbasin. (B) Simplified stratigraphy of the Kupferschiefer system in the Southern Permian Basin consisting of the uppermost Rotliegend sandstone (S1), Kupferschiefer (T1) and Zechstein Limestone (Ca1) (modified from Oszczepalski, 1999). (C) Geological map of the Saale subbasin (modified from Geologisches Landesamt Sachsen-Anhalt, 1993). The inset map highlights Cu-rich areas associated with the Rote Fäule alteration in the Sangerhausen-Mansfeld mining district (Geologisches Landesamt Sachsen-Anhalt, 2000). (D) Simplified stratigraphy of the Rotliegend and Zechstein Groups in the Saale subbasin. Abbreviations: AF = Apolda Fault, BH-GF = Blankenheim-Geiselatal Fault, FF = Finne Fault, HTF = Hornburger-Tiefen Fault, KH = Kyffhäuser, KHBF = Kyffhäuser NE-Boundary Fault, HF = Halle Fault, HVC = Halle Volcanic Complex, KF = Kelbra Fault, NF = Nebra Fault, Z1C = Zechstein conglomerate. (For interpretation of the references to color in this figure legend, the reader is referred to the web version of this article.)

Pieczyński et al., 2002). The Rote Fäule and associated sulfide mineralized zones are considered to represent a redox front, which has a lateral component in the German Kupferschiefer district and an oblique vertical component in the Polish Kupferschiefer district (Borg et al., 2012). The lateral sulfide zoning in these districts can extend several tens of kilometers and the vertical sulfide zoning in the Polish Kupferschiefer is on the scale of meters to tens of meters (Oszczepalski et al., 2019). The sulfide zones include a Cu zone mainly comprising chalcocite, bornite and chalcopyrite, an overlapping Zn—Pb zone comprising sphalerite and galena, and a pyrite zone (Borg et al., 2012).

A recent study on drill-core samples from the Saale subbasin (eastern Germany) has demonstrated that mineralization in the different sulfide zones formed primarily via the replacement of carbonate cement (Mohammedyasin et al., 2023a). The effective buffering capacity of the carbonate host rock means that any visible mineralogical and textural alteration is often highly cryptic in carbonate replacement systems (Hitzman et al., 2005; Selley et al., 2005). Fluid-rock interaction can produce isotopic haloes that can extend beyond the limit of the visible alteration (Beinlich et al., 2019). Previous studies in the Kupferschiefer district have reported $\delta^{13}\text{C}$ and $\delta^{18}\text{O}$ values from bulk-rock and mineral separate analyses of carbonate (Bechtel et al., 2000, 2001, 2002; Bechtel and Püttmann, 1991; Hammer et al., 1990). These studies have reported an overall decrease in carbonate $\delta^{13}\text{C}$ and $\delta^{18}\text{O}$ values towards the Rote Fäule from the sulfide zones, which have been linked to low temperature (100–120 °C) fluid-rock interaction (Bechtel et al., 2001, 2002; Bechtel and Püttmann, 1991). However, the expression of hydrothermal alteration in carbonate-bearing host rocks is also dependent on the composition of other mineralogical components such as detrital clasts and clay minerals, which are known to be variable across the boundary between the Rotliegend sandstone (S1) and the organic matter-rich, marine Kupferschiefer (T1).

The development of high-spatial resolution in situ methods (e.g., secondary ion mass spectrometry, SIMS) for analyzing the stable isotope composition of carbonate minerals now enables the investigation of samples with complex depositional, diagenetic, and hydrothermal paragenetic stages (Cui et al., 2021; Denny et al., 2020; Śliwiński et al., 2016; Sun et al., 2021). However, the value of microanalytical data is only fully maximized when it is coupled with detailed petrographic (e.g., cathodoluminescence, CL and scanning electron microscopy, SEM) characterization, which can be used to constrain paragenetic relationships (Barker and Dipple, 2019; Cui et al., 2021; Denny et al., 2020; Götze et al., 2013). This study investigates samples collected from three drill holes (Sangerhausen, Allstedt, Wallendorf) in the Saale subbasin (Fig. 1C), which intersect the S1, T1 and Ca1 units. All the three drill holes preserved fine-grained sulfides which are intergrown with and partially replace the calcite cement and veins. The Rote Fäule hematitic alteration is only intersected by the Sangerhausen drill hole. The origin of calcite (cement and veins) has been evaluated using a combination of CL and SEM petrography, EPMA major element chemistry, and SIMS $\delta^{13}\text{C}$ and $\delta^{18}\text{O}$ values. We use the data to critically assess the existing temperature-controlled isotopic fractionation model in calcite due to interaction with the mineralizing fluids in the Kupferschiefer districts (e.g., Bechtel et al., 2000, 2002) and provide a new interpretation for the observed microscale carbon and oxygen isotopic variabilities in calcite cement. Finally, we discuss the implications of the lack of hydrothermal isotopic alteration haloes in calcite cement around the carbonate replacement sulfide mineralization.

2. Geological background and previous studies

2.1. Geodynamic setting and sedimentary infill of the Southern Permian Basin

The Southern Permian Basin (SPB; Fig. 1A) is part of the intra-continental Central European Basin System (CEBS), which formed contemporaneously with the assembly of Pangea during the Late

Carboniferous to Early Permian (Plein, 1990; Ziegler, 1990). The crust beneath the CEBS comprises the Precambrian Baltica and the Precambrian–Paleozoic East European Cratons (Maystrenko et al., 2008; Ziegler, 1990). The NW–SE trending CEBS is superimposed on the SW–NE Westphalian foreland basin which developed in front of the Variscides (Baldschuhn et al., 2001). The varying crustal domains and the difference in the basin strikes played an important role in stress and strain localization during the post-Variscan evolution of the SPB (Maystrenko et al., 2008). The subsidence of the SPB during the latest Carboniferous–earliest Permian was dominantly related to wrench tectonics, intense magmatism and thermal relaxation of the lithosphere, and sediment loading (Breitkreuz et al., 2008; Pharaoh et al., 2010; Van Wees et al., 2000; Wilson et al., 2004; Ziegler, 1990).

The sedimentary history of the SPB started with fluviially deposited coarse conglomerates, lacustrine and/or carbonate sediments, and intercalated pyroclastic deposits of the latest Carboniferous to Early Permian Upper Rotliegend I (Gaitzsch, 1995; Schneider and Gebhardt, 1993). The Late Permian Upper Rotliegend II comprises continental siliciclastics and minor evaporites (Glennie and Buller, 1983). Local bioturbation and marine fauna in the uppermost part of the Rotliegend (S1) indicate the influence of a shallow marine, wave-dominated environment during the early Zechstein marine transgression (Legler et al., 2005; Tucker, 1991). This transgression resulted in seven sedimentary cycles (z1–z7, referred to in Germany as Werra, Staßfurt, Leine, Aller, Ohre, Friesland and Fulda) of the Zechstein Group (Fig. 1D, Radzinski, 2008). These sedimentary cycles are generally composed of mudstones at the base that progressively become carbonate-dominated in the middle and evaporites at the top (Kaiser et al., 2003; Stollhofen et al., 2008; Strohmenger et al., 1996; Tucker, 1991). The Upper Permian (Wuchiapingian) organic matter-rich, carbonaceous, mudstones of the Kupferschiefer (T1), overlying the uppermost Rotliegend (S1), or basal limestone (Border Dolomite), is the basal unit of the Werra Formation (Borg et al., 2012). The T1 can be subdivided into basinal, swell, and marginal facies, which reflect variability in the organic matter and carbonate content depending on the proximity to the basin margin (Paul, 2006; Ruebsam et al., 2017). The T1 unit is overlain by the Zechstein Limestone (Ca1) followed by the overlying anhydrite units.

Following the end of the Zechstein marine conditions, terrestrial redbeds of the Buntsandstein Group were deposited in some parts of the CEBS during the Early Triassic (e.g., Saale subbasin). The Buntsandstein Group is overlain by the marine, carbonate-dominated, Muschelkalk Group followed by a clastic succession of the Keuper; both units are Triassic in age (Stollhofen et al., 2008).

2.2. Overview of the Kupferschiefer system in the Saale subbasin

The Saale subbasin is located at the southern margin of the SPB (Fig. 1C). Historically, Cu and associated metals were mined in this subbasin from the Sangerhausen–Mansfeld mining district. A total of 2.6 Mt. of Cu and 14.2 kt of Ag were extracted from the Sangerhausen–Mansfeld district over the past eight centuries until mining ended in 1990 (Stedingk et al., 2002). The high-grade Cu mineralization (up to 19.9 wt%) in the Sangerhausen–Mansfeld mining district is restricted to the basal part of the T1 and spatially associated with the underlying Rote Fäule hematitic alteration, which is preserved in the uppermost part of the S1 (Sun and Püttmann, 1997, 2000). Short intervals (1 m each) from the Sangerhausen (102/80), Allstedt (11/86) and Wallendorf/Luppe (6/84) drill holes investigated in this study are located at the margin of the Rote Fäule alteration, Cu mineralized, and Zn—Pb mineralized parts of the Saale subbasin, respectively (inset Fig. 1C for locations). The Sangerhausen (max. Cu = 1.2 wt%) and Allstedt (Cu = 2.4 wt%) drill holes preserve Cu sulfides whereas the Wallendorf drill hole in the eastern part of the subbasin (~50 km from Allstedt) preserves Zn—Pb sulfides (Zn = 3.1 wt%, Pb = 1 wt%) (Mohammedyasin et al., 2023a). Mohammedyasin et al. (2023a) showed that the high-grade sulfide mineralization in the Saale subbasin formed via the replacement of carbonate and, to a

lesser extent, feldspar in the S1 and T1 units. The vein-type mineralization in this subbasin also formed as a replacement of calcite veins that cross-cut the host rocks (Mohammedyasin et al., 2023a). The main diagenetic and hydrothermal assemblages in the Kupferschiefer system that comprise the Rotliegend sandstone (S1), Kupferschiefer (T1) and Zechstein Limestone (Ca1) are summarized from Mohammedyasin et al. (2023a):

- Rotliegend sandstone (S1): The S1 is composed of detrital clasts including volcanic rock fragments, quartz and feldspar. There has been minimal compaction of the detrital clasts, and most of the volcanic and feldspar clasts were altered before calcite cementation. The intra- and intergranular calcite cement has occluded porosity, and forms overgrowths on rhombic dolomite and is mostly coeval with a patchy anhydrite cement. The high-grade sulfides (bornite, sphalerite, galena) replace and are intergrown with the calcite cement. The timing of pore-filling diagenetic illite probably overlaps with the sulfide formation.
- Kupferschiefer (T1): There is significant mineralogical variation up section in the T1, with the lower part dominated by phyllosilicates and the middle and upper parts by carbonates. Therefore, the T1 has been mineralogically subdivided as lower T1, middle T1 and upper T1. The lower T1 contains fine-grained laminations that are composed of clay mineral layers (mainly illite) rich in organic matter, and coarse-grained laminations that are composed of detrital quartz, feldspar and carbonate. Framboidal pyrite is ubiquitous in the fine-grained laminations. Carbonate (calcite and dolomite), and some feldspar, in the coarse-grained laminations, have been replaced by ore-stage Cu- and Zn–Pb sulfides. The middle and upper T1 are composed of detrital quartz and feldspar and have abundant carbonate cements (calcite and dolomite). The intergranular calcite cement in the T1 has been replaced by the ore-stage sulfides (bornite, sphalerite and galena).
- Zechstein Limestone (Ca1): The lowermost part of the Ca1 is composed of abundant rounded-subrounded dolomite, detrital quartz and feldspar, and phyllosilicates (mainly illite). The detrital clasts and dolomite have been cemented by very fine-grained (< 10 μm) intercrystalline calcite and minor anhydrite. The high-grade sulfides are mostly formed in vuggy pores.

2.3. Previous carbon and oxygen isotope studies in the Kupferschiefer district

2.3.1. Carbon isotopes of organic matter ($\delta^{13}\text{C}_{\text{org}}$)

A decreasing trend of $\delta^{13}\text{C}_{\text{org}}$ values in the T1 from the Cu zone through the overlapping Zn–Pb zone to the pyrite zone has been used to infer post-depositional organic matter degradation associated with the sulfide mineralization (Bechtel et al., 2000, 2001, 2002; Bechtel and Püttmann, 1991; Hammer et al., 1990). For example, the $\delta^{13}\text{C}_{\text{org}}$ values (–24.8‰ to –28.7‰, up-section) in the Lubin-Sieroszowice mining district (SW Poland) are higher in the Cu zone relative to the Zn–Pb zone, which has been linked to post-depositional oxidation of organic matter by ascending oxidizing, mineralizing fluids (Bechtel et al., 2002). Similarly, the $\delta^{13}\text{C}_{\text{org}}$ values in the T1 samples from the Richelsdorf Hills (Germany) are variable in different drill cores, but generally decrease up-section (Bechtel and Püttmann, 1991). The $\delta^{13}\text{C}$ values of the soluble (bitumen, –24.4‰ to –27.2‰) and insoluble (kerogen, –23.7‰ to –26.1‰) organic matter in the T1 samples from the Sangerhausen mining district also decreases upward (Bechtel et al., 2001).

2.3.2. Carbon and oxygen isotopes of carbonates

The $\delta^{13}\text{C}$ and $\delta^{18}\text{O}$ values of bulk carbonate (bulk-rock and mineral separate) in the Kupferschiefer districts generally increase from the Rote Fäule to the different sulfide zones (Bechtel et al., 2000, 2001, 2002; Bechtel and Püttmann, 1991). For example, the $\delta^{13}\text{C}$ (–3.4‰ to 4.1‰) and $\delta^{18}\text{O}$ (25‰ to 33.5‰) values of carbonate from the Sangerhausen

mining district generally increase from the Rote Fäule through the Cu-, overlapping Zn–Pb and pyrite zones, respectively (Bechtel et al., 2001).

The low $\delta^{13}\text{C}$ values of carbonate within, and adjacent to, the Rote Fäule from the Sangerhausen mining district and Richelsdorf Hills in Germany and the Polish Kupferschiefer districts have been explained by oxidation of organic matter derived from the T1 during the mineralization (Bechtel et al., 2000, 2001, 2002; Bechtel and Püttmann, 1991). The low $\delta^{13}\text{C}$ values of carbonate in the Rote Fäule from these districts have been used to argue for enhanced fluid-rock interactions caused by ascending, metal-bearing solutions and organic matter degradation in the T1 (Bechtel and Püttmann, 1991). This is based on the association of lower $\delta^{13}\text{C}$ values of carbonate with higher $\delta^{13}\text{C}_{\text{org}}$ values in the lower T1, compared to the other sulfide zones, which were interpreted for preferential fractionation of ^{12}C into calcite and ^{13}C into the organic matter during the mineralization. The systematic increase in $\delta^{13}\text{C}$ values in carbonate from the Cu zone into the Zn–Pb and pyrite zones, in contrast to $\delta^{13}\text{C}_{\text{org}}$ values, has been associated with a progressive decrease in organic matter degradation by the mineralizing fluids (Bechtel et al., 2000, 2002). The decrease in the extent of organic matter degradation has also been inferred from the decreasing trend in the temperature of maximum pyrolysis yield (T_{max}) values from the Rote Fäule through the Cu zone to the overlapping Zn–Pb zone in the T1 of the Lubin-Sieroszowice mining district in SW Poland (Bechtel et al., 2002).

The covariation between $\delta^{13}\text{C}$ and $\delta^{18}\text{O}$ values of carbonate in these previous studies from the German and Polish Kupferschiefer districts has been associated with temperature-controlled fluid-rock interactions between the carbonate and the mineralizing fluids (Bechtel et al., 2000, 2001, 2002; Bechtel and Püttmann, 1991). The decreasing $\delta^{18}\text{O}$ values of calcite towards the Rote Fäule in the Lubin-Sieroszowice mining district were interpreted to be the result of isotopic exchange between carbonate and isotopically distinct oxidizing brines at temperatures of 100–120 °C (Bechtel et al., 2002). In contrast, the progressive increase in $\delta^{13}\text{C}$ and $\delta^{18}\text{O}$ values in the bulk carbonate data towards the Cu zone through to the pyrite zone implies cooling of the mineralizing fluids along the pathways and, therefore, less interactions with carbonates and organic matter degradation.

3. Sampling and methods

3.1. Sampling and petrography

Samples for this study were selected from the Sangerhausen (SHN-102/80, $n = 17$), Allstedt (AST-110/86, $n = 17$) and Wallendorf/Luppe (WDF-6/84, $n = 13$) drill holes in the Saale subbasin, eastern Germany. All three drill holes intersect the uppermost part of the Rotliegend sandstone (S1), Kupferschiefer (T1) and Zechstein Limestone (Ca1) (Fig. 2). Samples were examined using a binocular microscope to document visible lithological and mineralogical variations. Standard polished thin- and thick sections were prepared from all samples ($n = 47$). Thin sections were examined using standard transmitted-reflected light microscopy. The distribution of carbonate cement was then examined using hot-cathode source cathodoluminescence (CL) equipped with a polarizing microscope, using 14 kV pre-set voltage and 0.1–0.2 mA current on carbon-coated (~5 nm) thin sections. Electron dispersive spectrometry analyses for detailed mineral identification and back-scattered electron (BSE) imaging for establishing mineral paragenesis were performed using a Zeiss ultra plus scanning electron microscope (SEM) at GFZ Potsdam (Germany). Electron dispersive spectrometry false-color elemental composite maps were also acquired to show the distribution of the different mineral phases. Electron dispersive spectrometry analyses were operated at 20 kV accelerated voltage.

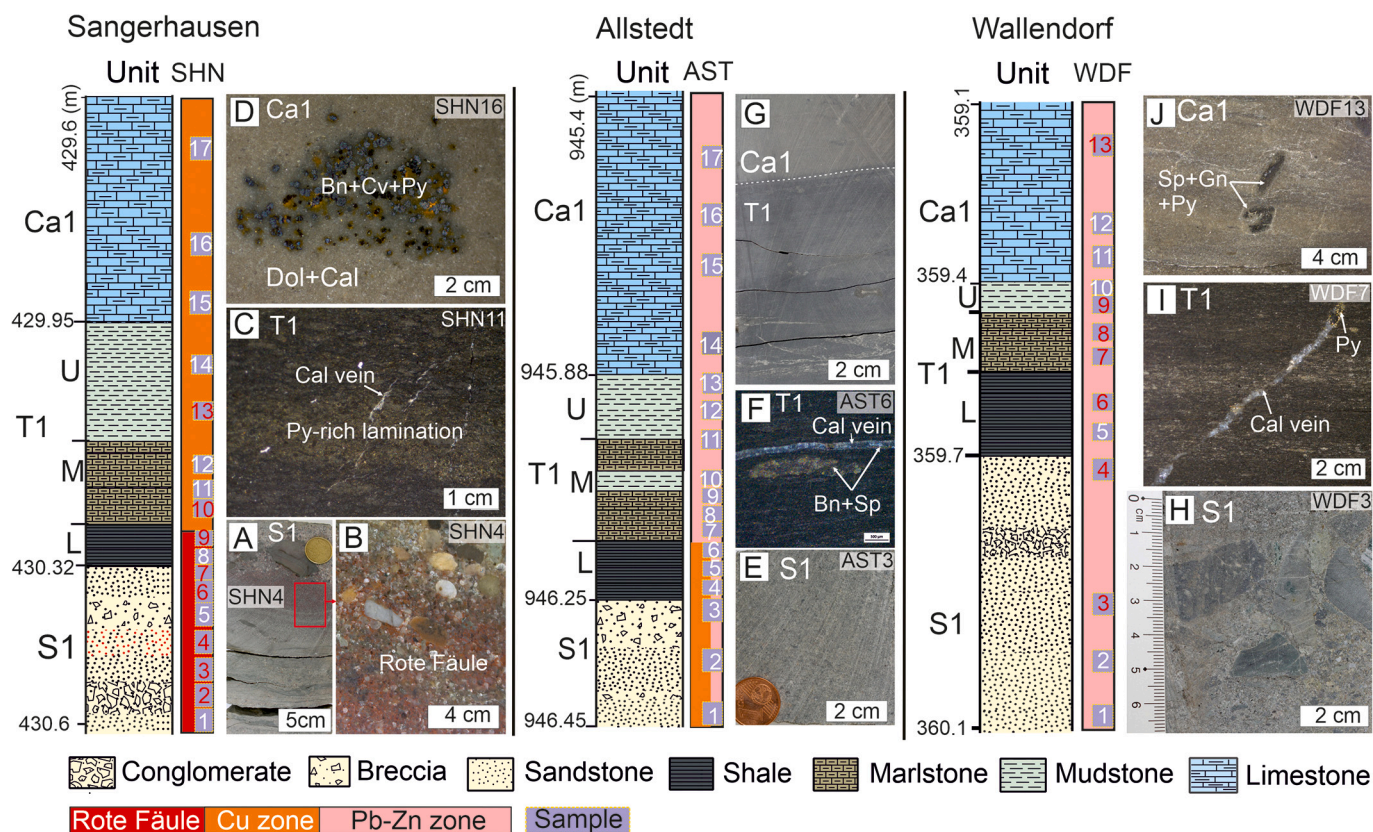


Fig. 2. Stratigraphic and lithological logs together with selected sample photographs for the three drill cores from Sangerhausen (SHN), Allstedt (AST) and Wallendorf (WDF). The sampled intervals are annotated numerically alongside each graphical log. (A) Drill core photo showing the red color in the Rote Fäule alteration in the Rotliegend sandstone (S1) (Samples SHN3 and SHN4). (B) Binocular image showing the red color Rote Fäule alteration in the S1 (Sample SHN4). (C) Binocular image of mineralized Kupferschiefer (T1) with host-rock cross-cutting calcite vein (Sample SHN11). (D) Binocular image showing vuggy pores filled with bornite (Bn), covellite (Cv) and pyrite (Py) in the Zechstein Limestone (Ca1) (Sample SHN16). (E) Drill core photo showing white sandstone without red color alteration in the S1 (Sample AST3). (F) Binocular image showing lateral calcite vein and a coarse-grained lens/lamination filled with bornite (Bn) and sphalerite (Sp) in the lower T1 (Sample AST6). (G) Drill core photo showing the boundary between the T1 and Ca. (H) Drill core photo showing brecciated clasts without red color alteration in the S1 (Sample WDF3). (I) Binocular image showing a host-rock cross-cutting calcite-pyrite vein in the middle T1 (Sample WDF7). (J) Binocular image showing vuggy pores filled with galena, sphalerite and pyrite in the Ca1. Samples analyzed by SIMS are indicated by red color. (For interpretation of the references to color in this figure legend, the reader is referred to the web version of this article.)

3.2. Major element analysis of carbonates by electron probe microanalyzer (EPMA)

Major elements (Ca, Mg, Fe, Mn, Na and Sr) were analyzed in calcite and dolomite using the JEOL Superprobe JXA-8230 electron probe microanalyzer (EPMA) equipped with wavelength-dispersive spectrometry (WDS) at GFZ Potsdam. Analyses were performed using a 5–20 μm beam size, 15 kV accelerating voltage, and 10 nA beam current, with a relatively short measurement time of 10–20 s (peaks) and 5–10 s (background). The measurements were conducted on carbon-coated thin sections using reference materials of dolomite (Ca, Mg), siderite (Fe), albite (Na), rhodonite (Mn), strontianite (Sr), BaSi_2O_5 (Ba), Cr_2O_3 (Cr), chalcopyrite (Cu) and gahnite (Zn). The detection limits of the method for these elements (in ppm = $\mu\text{g/g}$) were 780 (Ca), 720 (Mg), 820 (Fe), 650 (Na), 520 (Mn), 750 (Sr), 1100 (Ba, Zn), 1000 (Cr) and 850 (Cu).

3.3. Carbon isotope analysis of organic matter by isotope ratio mass spectrometry (IRMS)

The carbon isotope composition of organic matter ($\delta^{13}\text{C}_{\text{org}}$) was determined using the Delta V Advantage isotope ratio mass spectrometer (IRMS) at GFZ Potsdam. Powdered samples (3 mg each) were decalcified in a Ag-capsule with 3% HCl and then 20% HCl, and heated at 75 °C for 3 h. The analyses were calibrated using a certified reference material

(IAEA-CH-7) and a known internal laboratory sample (from Tiefer See Klocksin, TSK). The carbon isotope ratios are expressed relative to the Vienna Pee-Dee Belemnite (VPDB) in permil (‰). The repeatability of replicate analyses was better than 0.2‰ (1 standard deviation, 1s).

3.4. Carbon and oxygen isotope analyses of calcite by secondary ion mass spectrometry (SIMS)

A binocular microscope was used to identify regions of interest in polished thick sections. A micro drill press was used to extract the regions of interest (< 4 mm diameter), thereby enabling circular discs of 30 different samples to be mounted into two epoxy discs with a diameter of 25.4 mm. Mount 1 contains 15 circular discs from 8 samples of the Sangerhausen drill core and Mount 2 contains 15 circular discs from 7 samples of the Wallendorf drill core. The calcite reference materials UWC-3 ($\delta^{18}\text{O}_{\text{VSMOW}} = 12.49\text{‰}$, $\delta^{13}\text{C} = -0.91\text{‰}$; Kozdon et al., 2009) and IAEA-603 ($\delta^{18}\text{O}_{\text{PDB}} = -2.37\text{‰}$, $\delta^{13}\text{C} = 2.46\text{‰}$; IAEA, 2016) were mounted together with the rock samples; both reference materials and unknowns were located in the central part of the two epoxy discs (> 5 mm from the edges to avoid X-Y effects; Kita et al., 2009). The epoxy discs were cleaned with a high-purity ethanol ultrasonic bath and were then coated with a 35 nm thick Au layer. White-light profilometry was used to check the polishing relief (< 5 μm) in each sample. Before SIMS analyses, the two Au-coated mounts (10 nm) were SEM-BSE imaged to select the desired locations for the SIMS analysis on calcite. Oxygen and

carbon isotope analyses were performed during four analytical sessions using the CAMECA IMS 1280-HR Secondary Ion Mass Spectrometer (SIMS) at GFZ Potsdam (Supplementary Tables 3–5, Mohammedyasin et al., 2023b).

A ~ 2 nA (1st and 2nd sessions) and ~ 1 nA (3rd and 4th sessions) $^{133}\text{Cs}^+$ primary ion beam was focused to a 10 μm diameter spot with a total impact energy of 20 keV. Before data collection, each analytical target was sputtered for 75 s (65 s in the 3rd session) with a 15 μm raster to remove the Au-coat. Data collection used an 8 μm raster to ensure a flat-bottom crater geometry. Additionally, adjustment of the electron multiplier (EM) and sample high-voltages was also performed during carbon isotope analysis. The field aperture was set to $4000 \times 4000 \mu\text{m}$ (resulting in a field of view of 40 μm) and the contrast aperture had a 400 μm diameter. The energy slit had a width of 40 eV and it was mechanically positioned 5 V below maximum transmission at the start of each of the analytical sequences. Data were collected in multicollection mode using two Faraday cup detectors for oxygen isotope analysis (L'2 for $^{16}\text{O}^-$, H'2 for $^{18}\text{O}^-$) and a Faraday cup/Axial Electron multiplier (Mono-EM) configuration for carbon isotope analysis (L'2 for $^{12}\text{C}^-$, Mono-EM for $^{13}\text{C}^-$). The entrance slit had a width of 82–110 μm for carbon isotope analysis and 120 μm for oxygen isotope analysis, while the exit slit had a width of 270–300 μm for carbon isotope analysis and 500 (L'2)-300 (EM) μm for oxygen isotope analysis. The count rates in UWC-3 were typically 1.6 to 3.0×10^9 counts per second (cps) on $^{16}\text{O}^-$ and 1.3 to 1.7×10^7 cps on $^{12}\text{C}^-$. The mass resolution of the SIMS was set at $M/\Delta M \approx 2000$ (O) and 3200 (C), at 10% of peak height. Each analysis lasted ~ 3 (O) to 4 (C) minutes including pre-sputtering, auto-centering and data acquisition routines, which consisted of 20 integrations of 4 s each for oxygen isotopes and 30 integrations of 4 s each for carbon isotopes.

The instrumental mass fractionation (IMF) and signal drift with time were monitored by repeated measurements throughout the analytical sessions in grains of the UWC-3 calcite reference material. A time-dependent drift was observed only at the start of the 3rd session during carbon isotope analysis in Mount 1, and measured isotope ratios were therefore corrected for drift. The repeatability (1 standard deviation, 1s) varied from $\pm 0.13\%$ to $\pm 0.19\%$ for the oxygen isotopes and from $\pm 0.25\%$ to $\pm 0.36\%$ for the carbon isotopes. We used the IAEA-603 calcite reference material as a quality control to assess the accuracy of the analytical bias correction defined by the results from the UWC-3 reference material. The corrected $\delta^{13}\text{C}$ and $\delta^{18}\text{O}$ values of IAEA-603 were within 2s uncertainty in UWC-3 from the published value. The reported errors are therefore better than $\pm 0.20\%$ (1SE) for $\delta^{18}\text{O}$ values and $\pm 0.40\%$ (1SE) for $\delta^{13}\text{C}$ values. Oxygen isotope ratios are expressed relative to the Vienna Standard Mean Ocean Water (VSMOW; $^{18}\text{O}/^{16}\text{O} = 0.0020052$; Baertschi, 1976) and carbon isotope ratios are expressed relative to the Vienna Pee-Dee Belemnite (VPDB; $^{13}\text{C}/^{12}\text{C} = 0.0112372$; Craig, 1957, Allison et al., 1995).

All SIMS spots were SEM-BSE imaged and analyses were rejected if the corresponding pits touched other mineral phases, cracks, or porosity. Finally, 267 (130 for carbon and 137 for oxygen) analyses out of the total 404 (227 for carbon and 177 for oxygen) isotope analyses were considered trustworthy for further interpretation.

4. Results

4.1. Petrography of carbonates

Cathodoluminescence (CL) and BSE images show the distribution and morphology of carbonate (dolomite and calcite) cements in samples from the S1, T1 and Ca1. In the S1 samples, calcite is the dominant carbonate phase and occurs in both intra- and intergranular pores (Fig. 3A, B). The calcite cement in both types of pore spaces has a bright red CL luminescence (Fig. 3C, D). The zoning in the intergranular calcite in the S1 samples from the Sangerhausen drill core is only apparent in BSE images (Fig. 3E-F). Hematite is intergrown with calcite cement,

mostly at its rims (Fig. 3E-F). Minor rhombic dolomite (~ 5 – $10 \mu\text{m}$) is overgrown by intergranular calcite cement in the S1 samples in all drill cores (e.g., Fig. 3F). Dolomite has a slightly darker red CL color compared to calcite (Fig. 4A). Additionally, the S1 samples in the Sangerhausen drill core also contain rhombic dolomite cemented by calcite (\pm trace ankerite) in large dolomitized clasts (Fig. 4B-D).

In samples from the T1, the calcite cement is fine-grained ($< 20 \mu\text{m}$), and overgrows on rhombic dolomite ($< 10 \mu\text{m}$) (Fig. 5A-D). However, the resolution of the CL microscope did not allow the fine-grained calcite and dolomite to be distinguished from each other. The calcite veins mostly occur in the Wallendorf drill core samples. In contrast to the calcite cement, the calcite veins have darker red and brighter red CL luminescence colors (Fig. 5E). In Fig. 5F, a cross-cutting calcite vein has internal zoning with brighter and darker red CL luminescence colors.

In samples from the Ca1, dolomite has a red luminescence CL color (Fig. 6A). Rhombic dolomite crystals (~ 5 – $10 \mu\text{m}$) have been cemented by fine-grained calcite cement ($< 5 \mu\text{m}$) (Fig. 6B). In the Allstedt drill core samples, host rock cross-cutting anhydrite veins, with minor calcite (yellow CL luminescence color), have blue CL luminescence color (Fig. 6C-E).

4.2. Major element chemistry of carbonates

The carbonate chemistry of samples from the three drill cores is available in the Supplementary data (Mohammedyasin et al., 2023b). The CaCO_3 - MgCO_3 - $(\text{Fe,Mn})\text{CO}_3$ concentrations of calcite and dolomite plot near the stoichiometric calcite and dolomite compositions, respectively (Fig. 7). Both styles of calcite (cement and veins) contain relatively minor concentrations of MgCO_3 , FeCO_3 and MnCO_3 which are below 8.6 mol%, 2.0 mol% and 6.8 mol%, respectively. Dolomite from the three units contains relatively minor concentrations of FeCO_3 (mean = 0.7 mol%) and MnCO_3 (mean = 0.8 mol%).

The Mn concentration is higher in calcite than dolomite and varies slightly between drill cores (Fig. 8A). For example, the Mn concentration is slightly higher in samples from the Sangerhausen drill core compared to the Wallendorf and Allstedt drill cores (Fig. 8A). In contrast, the Na and Sr concentrations are relatively higher in dolomite than calcite (Fig. 8B-D). Trace elements such as Ba, Cr, Cu and Zn are mostly below the detection limit in both mineral phases.

4.3. Carbon isotope composition of organic matter ($\delta^{13}\text{C}_{\text{org}}$)

The $\delta^{13}\text{C}_{\text{org}}$ values for samples from the three drill cores are available in the Supplementary data (Mohammedyasin et al., 2023b) and summarized in Fig. 9. The $\delta^{13}\text{C}_{\text{org}}$ values in the three drill cores have a narrow range (-27.4% to -25.8% , in VPDB hereafter). Vertical profiles of $\delta^{13}\text{C}_{\text{org}}$ values in the three drill cores are relatively similar, with the lowest values mostly confined to the middle T1 (Fig. 9A-C). The correlations between TOC and $\delta^{13}\text{C}_{\text{org}}$ in the T1 samples differ between drill cores, ranging from weak ($r^2 = 0.21$ to 0.24) in samples from the Sangerhausen and Allstedt drill cores to moderate ($r^2 = 0.53$) in those from the Wallendorf drill core (Appendix Fig. A1). In the Ca1 samples, $\delta^{13}\text{C}_{\text{org}}$ values were only measured in samples from the Wallendorf drill core (range -27% to -26% , Fig. 9C) as organic carbon was below the detection limit in samples from the other drill cores.

4.4. In situ $\delta^{13}\text{C}$ and $\delta^{18}\text{O}$ values of calcite

The $\delta^{13}\text{C}$ and $\delta^{18}\text{O}$ values for calcite in samples from the Sangerhausen and Wallendorf drill cores are available in the Supplementary data (Mohammedyasin et al., 2023b) and summarized in Fig. 10. The samples from the Allstedt drill hole were not considered for SIMS analysis because of a lack of sample material. The $\delta^{13}\text{C}$ values are in VPDB and the $\delta^{18}\text{O}$ values are in VSMOW unless otherwise stated hereafter. The $\delta^{13}\text{C}$ and $\delta^{18}\text{O}$ values of calcite cement in the S1 and T1 have high microscale variabilities ($> 10\%$ for both isotopes) (Fig. 10A,

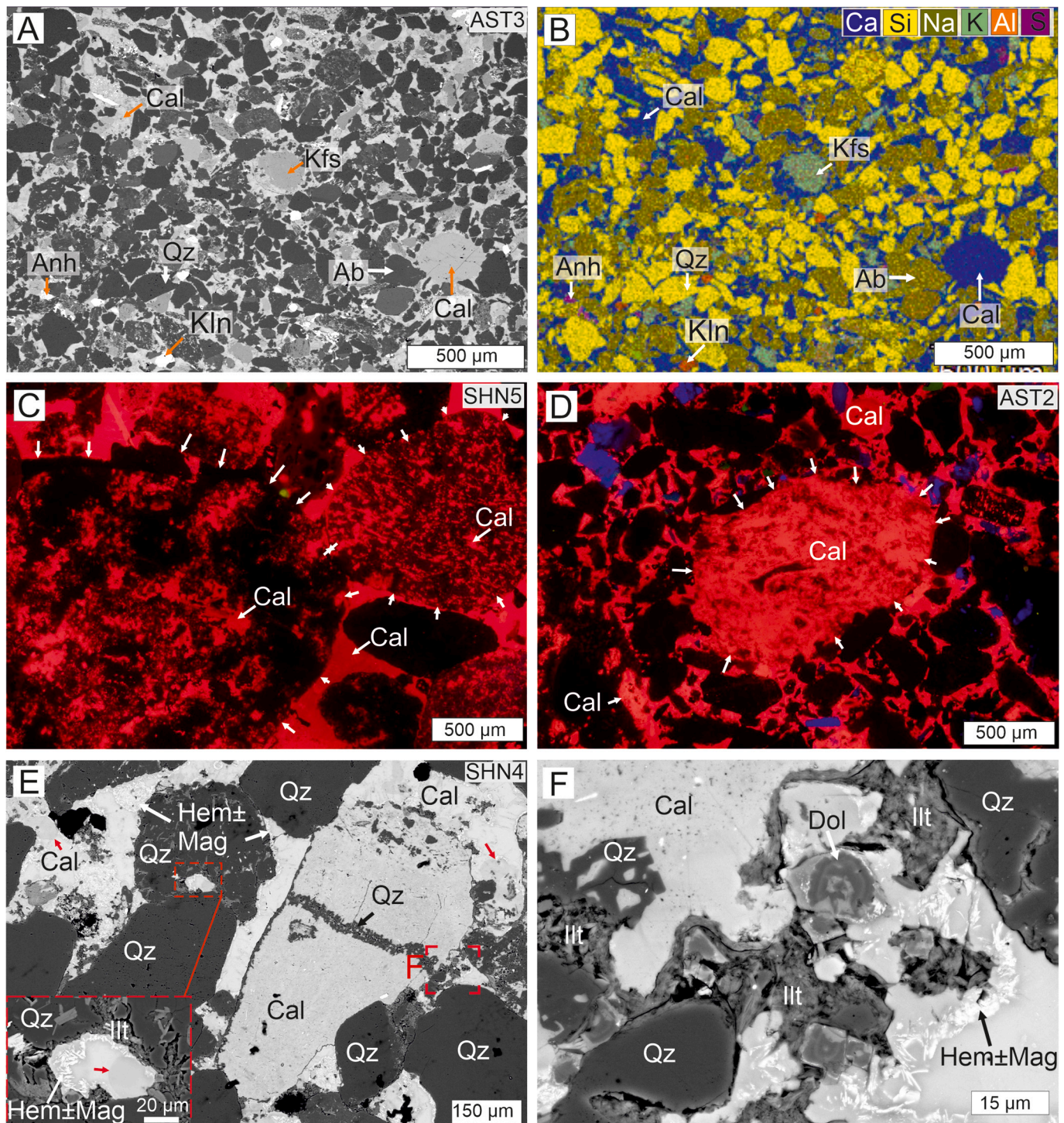


Fig. 3. (A, B) Backscattered electron (BSE) image and electron dispersive spectrometry (EDS) false-color elemental composite map showing the distribution of detrital quartz (Qz), albite (Ab) and K-feldspar (Kfs), extensive calcite (Cal) cement and minor anhydrite (Anh) and kaolinite (Kln) in the Rotliegend sandstone (S1) (Sample AST3). (C, D) Cathodoluminescence (CL) images showing bright red color calcite cement formed as intra- and intergranular pore filling in the Sangerhausen (Sample SHN5) and Allstedt (Sample AST2) drill cores. The white arrows highlight the boundary of detrital clasts that are partially or nearly completely replaced by calcite. (E) BSE image showing detrital clast replaced by calcite and intergranular calcite cement (Sample SHN4). The inset shows calcite cement zoning with the outer zone having hematite (\pm magnetite, Mag). The red arrows highlight internal zoning in intergranular calcite cement. (F) BSE image showing a detailed view of hematite (Hem) intergrown with one of the intergranular calcite cement zones, showing an overlapping paragenetic relationship. The meshwork illite (Ill) formed as an intergranular pore-filling phase, after calcite dissolution. Key for the EDS false color elemental map: Al = kaolinite, Ca = calcite, K = K-feldspar, Na = albite, S = anhydrite, Si = quartz. (For interpretation of the references to color in this figure legend, the reader is referred to the web version of this article.)

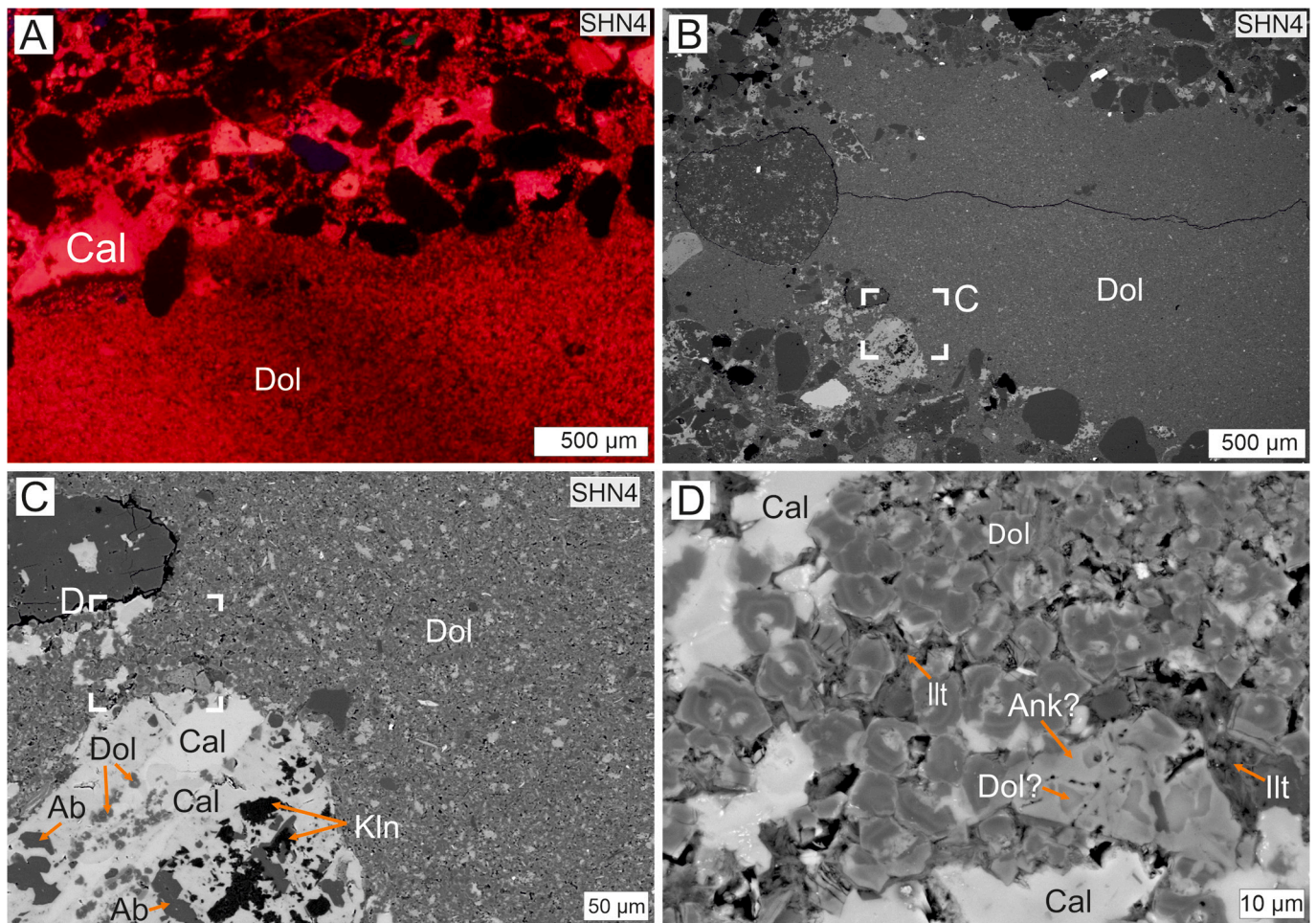


Fig. 4. (A) CL image showing calcite (Cal) and dolomite (Dol) with brighter and darker red CL colors, respectively in the S1 (Sample SHN4). (B) BSE image showing a large cavity filled with dolomite crystals (Sample SHN4). (C) BSE image showing altered volcanic rock fragment with albite (Ab) replaced by the intergrowth of dolomite, calcite and kaolinite (Kln), surrounded with macropore-filling rhombs of dolomite with minor calcite cement (Sample SHN4). (D) BSE image showing a detailed view of macropore-filling rhombic dolomite with calcite cement (\pm trace ankerite, Ank) and illite (Ill). (For interpretation of the references to color in this figure legend, the reader is referred to the web version of this article.)

B). In general, the in situ isotope analysis of calcite cement in this study reproduces the overall range of $\delta^{18}\text{O}$ ($\sim 18\text{‰}$ to 31‰) and $\delta^{13}\text{C}$ ($\sim 0\text{‰}$ to -10‰) values of calcite mineral separate from the Polish Basin (Bechtel et al., 2000, 2002). However, the $\delta^{13}\text{C}$ values of calcite cement in this study have shifted by 5‰ to lower values compared to previous studies from the Polish Basin.

The $\delta^{13}\text{C}$ and $\delta^{18}\text{O}$ values of intra- and intergranular calcite cement in the S1 samples from the two drill cores largely overlap (Figs. 11A, 12A, B). In samples from the Sangerhausen drill core, the $\delta^{13}\text{C}$ values of calcite cement in the S1 are between -10.1‰ and 4.3‰ (mean = -4.6‰ , $n = 44$) and $\delta^{18}\text{O}$ values are between 18.3‰ and 38.7‰ (mean = 24.4‰ , $n = 53$) (Fig. 10A). Three spot analyses from intragranular calcite cement in the Sangerhausen drill core have high $\delta^{13}\text{C}$ values, i.e., 3.5‰ in SHN2 and 4.3‰ and 3.7‰ in SHN7 with paired $\delta^{18}\text{O}$ values of 29.2‰ , 27.5‰ , 38.7‰ , respectively (Fig. 11A, Appendix Fig. A2A, B). In samples from the Wallendorf drill core, the $\delta^{13}\text{C}$ values of calcite cement are between -12.9‰ and -0.3‰ (mean = -5.6‰ , $n = 20$) and $\delta^{18}\text{O}$ values are between 18.8‰ and 27.8‰ (mean = 23.6‰ , $n = 18$) (Fig. 10B).

The $\delta^{13}\text{C}$ and $\delta^{18}\text{O}$ values of calcite cement in the T1 are also relatively similar in the Sangerhausen and Wallendorf drill cores (Figs. 11B; 12C, D). The $\delta^{13}\text{C}$ values of calcite cement in the Sangerhausen samples are between -6.8‰ and -3.0‰ (mean = -5.4‰ , $n = 6$) and $\delta^{18}\text{O}$ values between 26.9‰ and 30.7‰ (mean = 28.9‰ , $n = 2$). In the

Wallendorf samples, the $\delta^{13}\text{C}$ values of calcite cement are between -10.3‰ and 0.7‰ (mean = -4.3‰ , $n = 17$) and the $\delta^{18}\text{O}$ values are between 11.7‰ and 29.5‰ (mean = 23.7‰ , $n = 21$).

The $\delta^{13}\text{C}$ and $\delta^{18}\text{O}$ values of calcite veins in the T1 and Ca1 from the two drill cores fall on a similar trend (Figs. 11C, 13A-D). The $\delta^{13}\text{C}$ values of calcite veins in the T1 from the Sangerhausen drill core are between -2.2‰ and -1.2‰ (mean = -1.7‰ , $n = 8$) and $\delta^{18}\text{O}$ values are between 20.3‰ and 20.8‰ (mean = 20.6‰ , $n = 7$). The $\delta^{13}\text{C}$ values of calcite veins in the T1 from the Wallendorf drill core are between -14.8‰ to -1.4‰ (mean = -8.9‰ , $n = 27$) and $\delta^{18}\text{O}$ values are between 21.1‰ and 25.2‰ (mean = 23.5‰ , $n = 26$) (Fig. 11C). In the Ca1, calcite veins were only analyzed in the Wallendorf drill core where the $\delta^{13}\text{C}$ values are between -6.2‰ and -0.8‰ (mean = -3.0‰ , $n = 8$) and the $\delta^{18}\text{O}$ values are between 18.6‰ and 23.7‰ (mean = 21.9‰ , $n = 10$).

5. Discussion

The variabilities in chemical and isotopic ($\delta^{13}\text{C}$ and $\delta^{18}\text{O}$) compositions in calcite cement could be attributable to variable pore fluid chemistry during precipitation or fluid-rock interactions related to diagenetic and hydrothermal processes (Reis et al., 2019; Schobben et al., 2016; Śliwiński et al., 2016). In the following sections, we discuss the CL response and major element chemistry of carbonates, the $\delta^{13}\text{C}_{\text{Org}}$

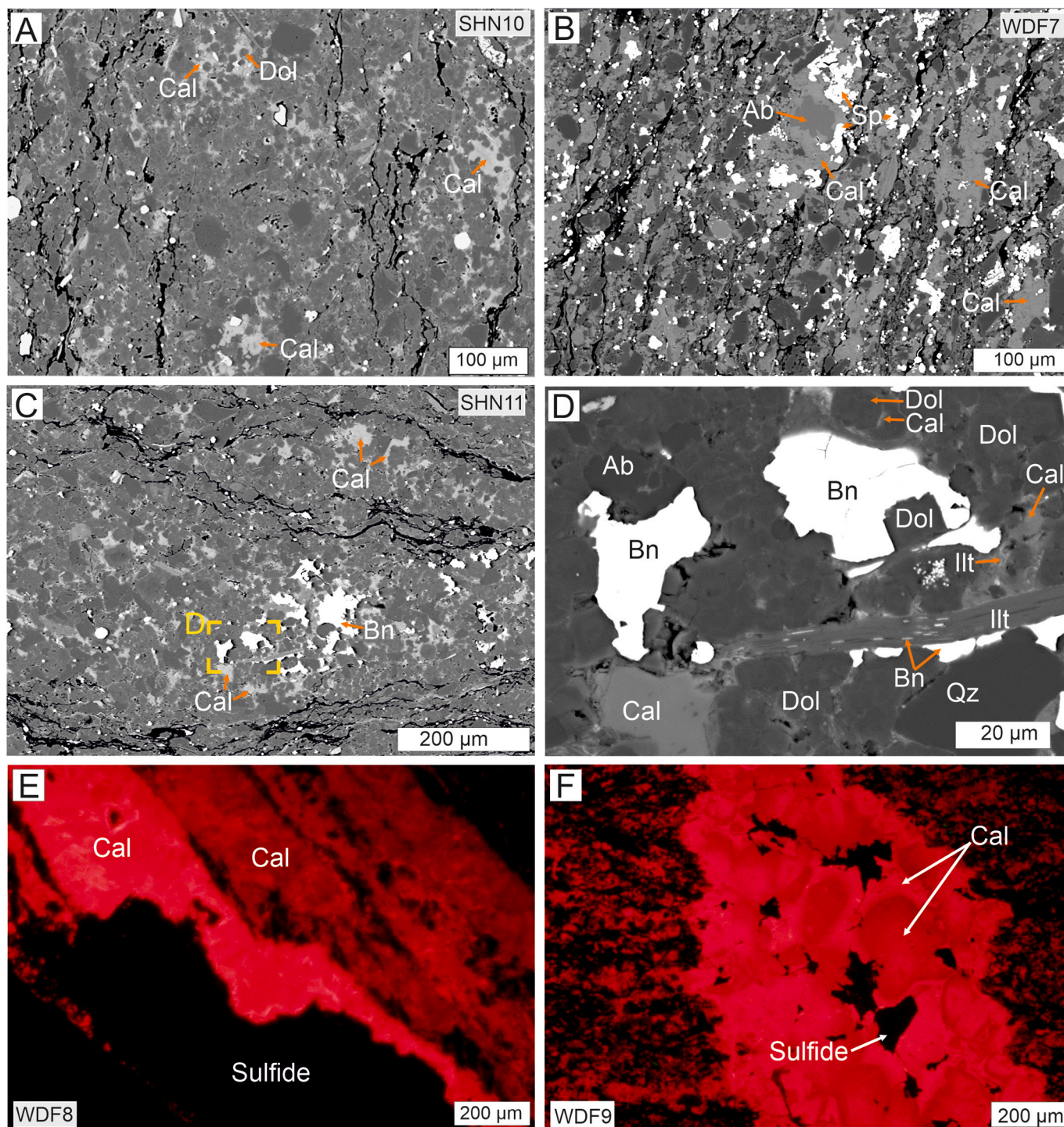


Fig. 5. (A, B) BSE images showing the distribution of calcite (Cal) cement in the middle Kupferschiefer (T1) from the Sangerhausen (Sample SHN10) and Wallendorf (WDF7) drill cores. The fine-grained calcite cement is mostly overgrown on rhombic dolomite (Dol) or detrital albite (Ab). The calcite cement is partially replaced by sphalerite (Sp). (C, D) BSE image showing the distribution and replacement of calcite cement by bornite (Bn) in the middle T1 from the Sangerhausen drill core (Sample SHN11). (E) CL image showing a host rock cross-cutting calcite vein with darker and brighter red CL color. (F) CL image showing a host rock cross-cutting calcite vein (darker red) internally cemented by calcite cement (brighter red). (For interpretation of the references to color in this figure legend, the reader is referred to the web version of this article.)

values, and microscale $\delta^{13}\text{C}$ and $\delta^{18}\text{O}$ values of calcite cement and veins to constrain their origins. We also assess if the isotopic composition of the calcite cement has been altered by hot, Cu mineralizing fluids.

5.1. CL response and major element chemistry of carbonates

The CL response in carbonate minerals is mainly a function of activating (e.g., Mn^{2+}) and quenching (e.g., Fe^{2+}) ions, which substitute for Ca^{2+} in the calcite crystal lattice (Baele et al., 2019; Machel and Burton, 1991; Marshall, 1988). The calcite cements in the S1, T1 and Ca1 are

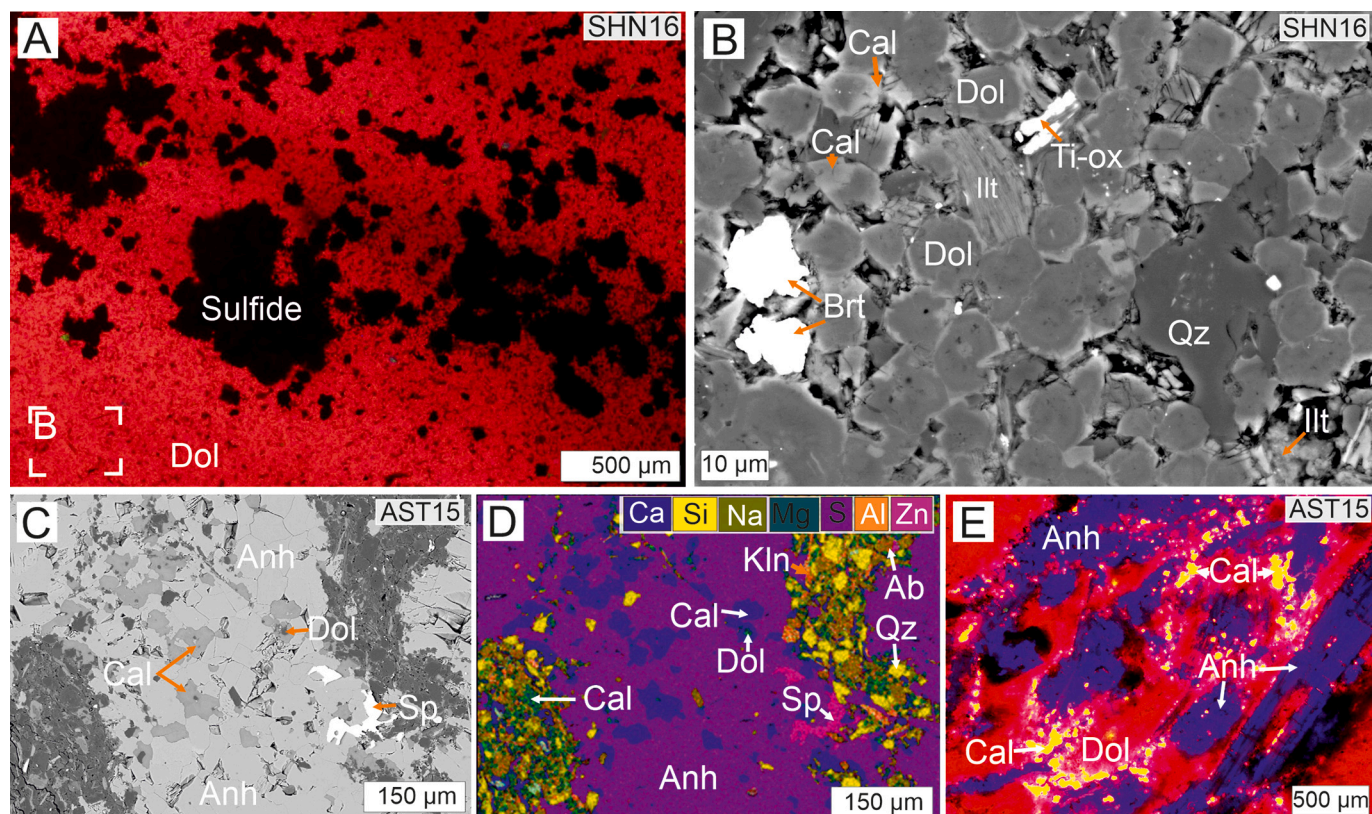


Fig. 6. (A) CL image showing dolomite (Dol) and vuggy pores filled with sulfides in the Zechstein Limestone (Ca1) from Sangerhausen drill core (Sample SHN16). (B) BSE image showing a detailed view of euhedral-subhedral dolomite crystals cemented by fine-grained calcite (Cal) cement, illite (Ill) and trace barite (Brt) (Sample SHN16). (C, D) BSE and false-color EDS images showing anhydrite (Anh) vein with calcite and the host rock dolomite rich in quartz, albite and phyllosilicates in the Ca1 from the Allstedt drill core (Sample AST15). (E) CL image showing anhydrite vein, dolomite and calcite with blue, darker red and yellow CL luminescence color, respectively, in the Ca1 from the Allstedt drill core (Sample AST15). (For interpretation of the references to color in this figure legend, the reader is referred to the web version of this article.)

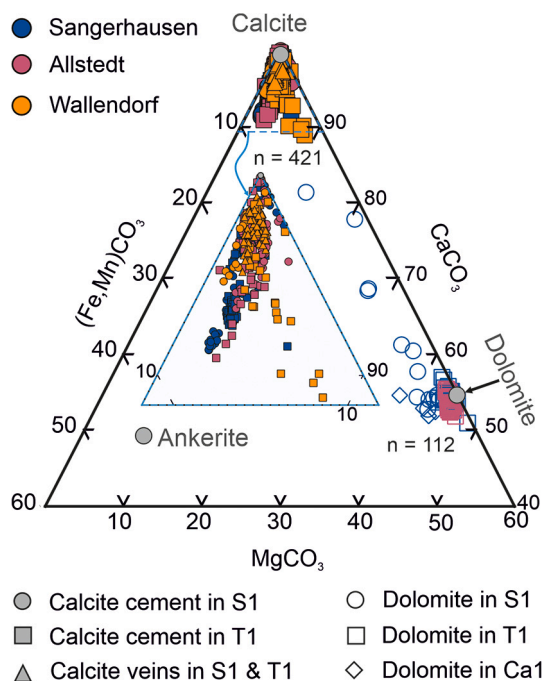


Fig. 7. Ternary diagram of $\text{CaCO}_3\text{-(Fe,Mn)CO}_3\text{-MgCO}_3$ (EPMA, mol%) showing endmember calcite and dolomite in samples from the Rotliegend sandstone (S1), Kupferschiefer (T1) and Zechstein Limestone (Ca1) in the Sangerhausen, Allstedt and Wallendorf drill cores.

characterized by similar CL luminescence (Figs. 3C, D, 4A), which suggests that the calcite cements have similar Ca, Mn and Fe chemistry (Pierson, 1981). This also applies to both the intra- and intergranular calcite cement in the S1 that have similar CL luminescence. The CL observations in calcite are consistent with the high Mn and low Fe concentrations recorded in the major element data (Fig. 8A). The slight difference in CL intensity between dolomite and calcite cement is the result of lower Mn and higher Fe in the dolomite than the calcite (Fig. 8A-D). The major element composition of dolomite in the S1, T1 and Ca1 samples from the two drill cores is also similar, reflecting their origin from fluids of similar chemistry.

The calcite veins have almost similar CL responses as the calcite cements (Fig. 5E, F). The cross-cutting calcite veins in the T1 samples from the Wallendorf drill core show internal zoning characterized by darker and brighter red CL luminescence, which is not apparent in the BSE images (Fig. 5E, F). The internal zoning in calcite veins is consistent with the microscale variabilities in Mn and Fe concentrations in these veins (Fig. 8A). However, the similarities in the CL response and major element chemistry between calcite cement and veins indicate their formation from fluids with similar major element chemistry, although the crosscutting relationship indicates they were not coeval.

5.2. The $\delta^{13}\text{C}_{\text{org}}$ trend in different drill cores

Previous studies in the Kupferschiefer district have described post-depositional organic matter degradation associated with sulfide mineralization (Bechtel et al., 2000, 2001, 2002; Bechtel and Püttmann, 1991; Hammer et al., 1990). In the Saale subbasin, organic matter degradation is not only linked with the mineralizing event but also with early

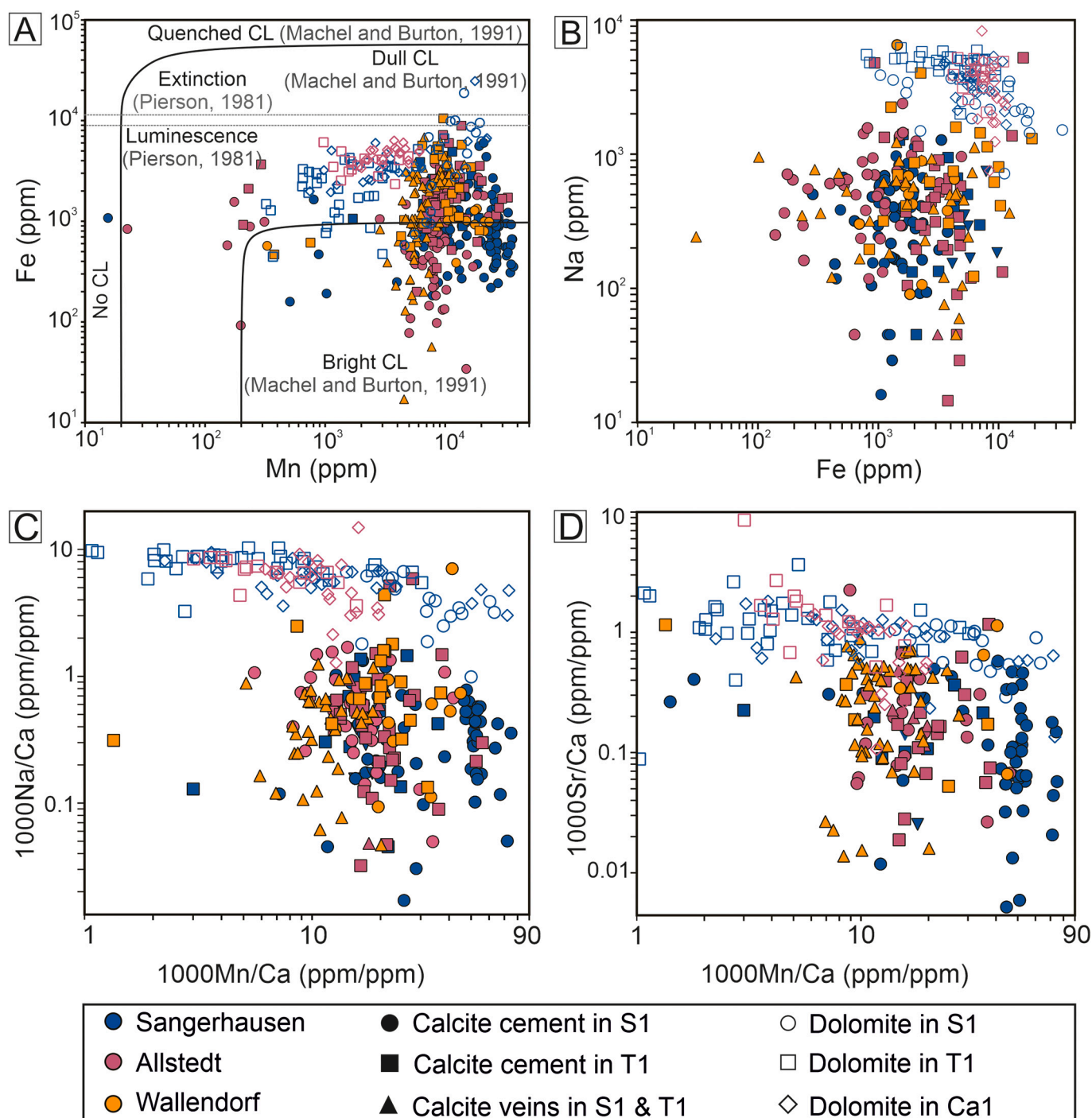


Fig. 8. (A) Plot of Mn (ppm) vs. Fe (ppm) showing that both calcite and dolomite fall on the luminescent field of Pierson (1981), and that calcite has more bright CL than dolomite where quenched, dull and bright CL fields are from Machel and Burton (1991). (B) Bivariate plot of Fe (ppm) vs. Na (ppm). (C) Bivariate plot of 1000Mn/Ca (ppm/ppm) vs. 1000Na/Ca (ppm/ppm). (D) Bivariate plot of 1000Mn/Ca (ppm/ppm) vs. 1000Sr/Ca (ppm/ppm).

diagenetic carbonate formation. Within analytical uncertainties, the low $\delta^{13}\text{C}_{\text{org}}$ values in the carbonate-rich intervals, mostly in the middle T1 (Fig. 9), can probably be explained by the preferential fractionation of ^{13}C from the organic matter into the precipitating carbonate minerals during early diagenesis. The reason for the slight difference in the $\delta^{13}\text{C}_{\text{org}}$ trend between the dolomite-dominated Sangerhausen and Allstedt drill cores and the calcite-dominated Wallendorf drill core is not clear. One possible explanation could be the rate of organic matter oxidation, i.e., higher organic matter degradation favored dolomite precipitation and lower organic matter degradation favored calcite

precipitation (e.g., Mozley and Burns, 1993). In contrast, the highest $\delta^{13}\text{C}_{\text{org}}$ value is preserved in the lowermost T1 of the Sangerhausen drill core (Fig. 9A), which also preserves the Rote Fäule alteration and may indicate the preferential fractionation of ^{12}C into the fluid, meaning more residual ^{13}C remains in the organic matter during progressive organic matter degradation (see Bechtel et al., 2002).

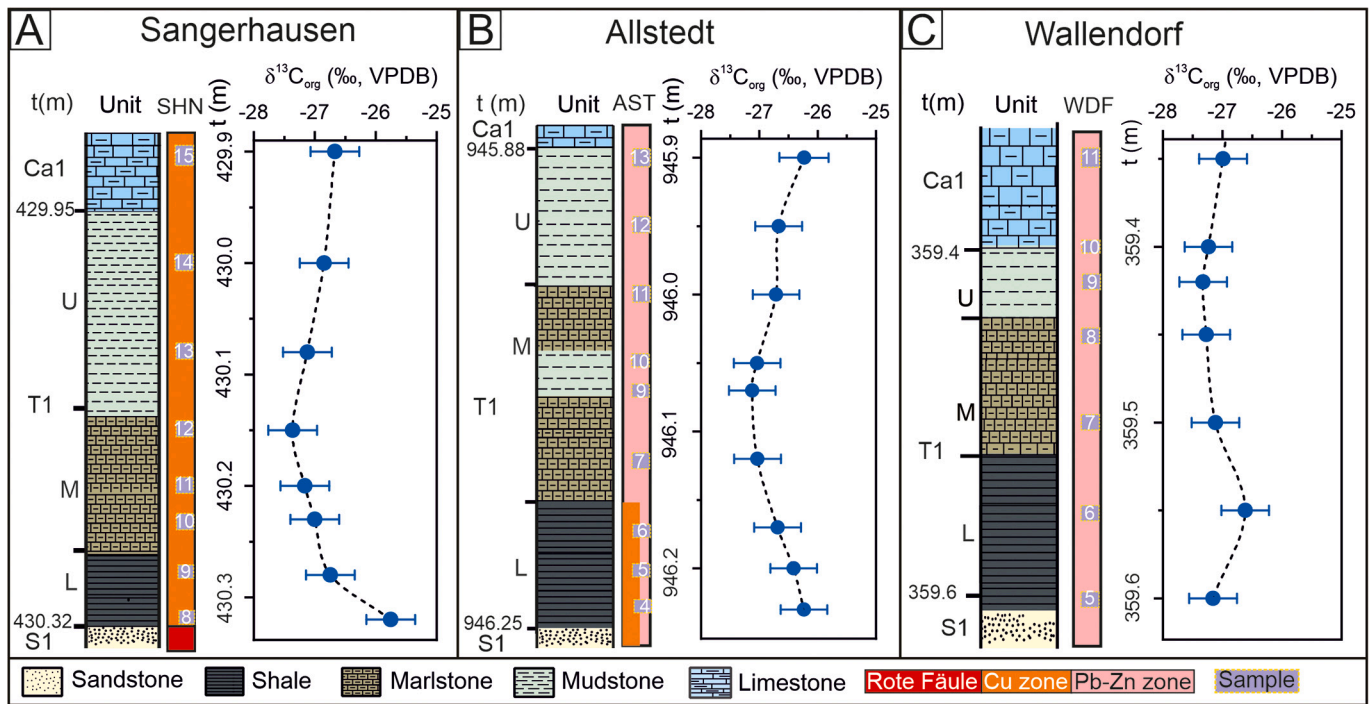


Fig. 9. Down-hole plot of $\delta^{13}\text{C}_{\text{org}}$ values mainly in samples from the Kupferschiefer (T1) in the (A) Sangerhausen (SHN), (B) Allstedt (AST) and (C) Wallendorf (WDF) drill cores. S1 = Rotliegend sandstone, Ca1 = Zechstein Limestone.

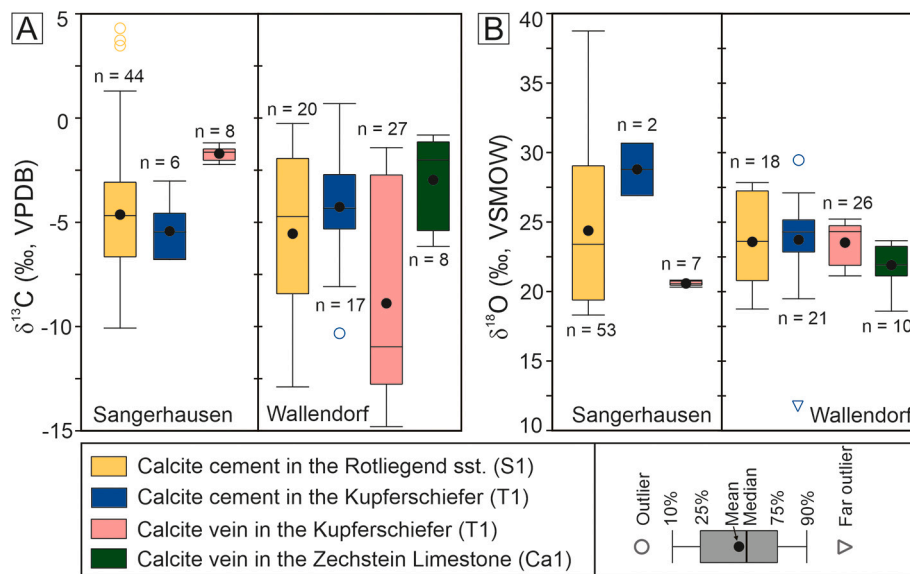


Fig. 10. Box and whisker plot of $\delta^{13}\text{C}$ and $\delta^{18}\text{O}$ values of calcite (cement and veins) in samples from the Rotliegend sandstone (S1), Kupferschiefer (T1) and Zechstein limestone (Ca1) in the (A) Sangerhausen and (B) Wallendorf drill cores.

5.3. Origin of calcite cement and veins

5.3.1. Sources of carbon for calcite cement and veins

The general overlap in the isotopic composition of the calcite cement from both units (S1 and T1) and drill cores is consistent with the similarity in major element chemistry, and indicates the calcite cement was derived from fluids of similar composition (Fig. 11A, B). The $\delta^{13}\text{C}$ values of calcite cement plot between the $\delta^{13}\text{C}$ values of the Permian Zechstein seawater (inferred from the Zechstein brachiopods; Korte et al., 2005) and organic matter (Hoefs, 2019). In general, calcite precipitated from alkalinity derived from seawater has a $\delta^{13}\text{C}$ value of close to 0‰ whereas calcite precipitated from the breakdown of organic matter and

hydrocarbons has a $\delta^{13}\text{C}$ value of around -20‰ (e.g., Fayek et al., 2001). Therefore, the alkalinity of the calcite cement in the S1 and T1 samples was sourced from seawater-derived fluids and organic matter degradation in the T1. The two positive $\delta^{13}\text{C}$ values (up to 4.3‰) from the S1 samples in the Sangerhausen drill core have similar isotopic values to the Zechstein brachiopods and could represent the earliest formed calcite cement (Fig. 11A).

The negative $\delta^{13}\text{C}$ values (down to -14.8‰) in calcite veins indicate carbonate alkalinity derived from the oxidation of organic matter in the T1. The calcite vein in the lower T1 from the Sangerhausen drill core has relatively higher $\delta^{13}\text{C}$ values than the calcite veins in the middle T1 and Ca1 samples from the Wallendorf drill core (Fig. 13A, B). However, in

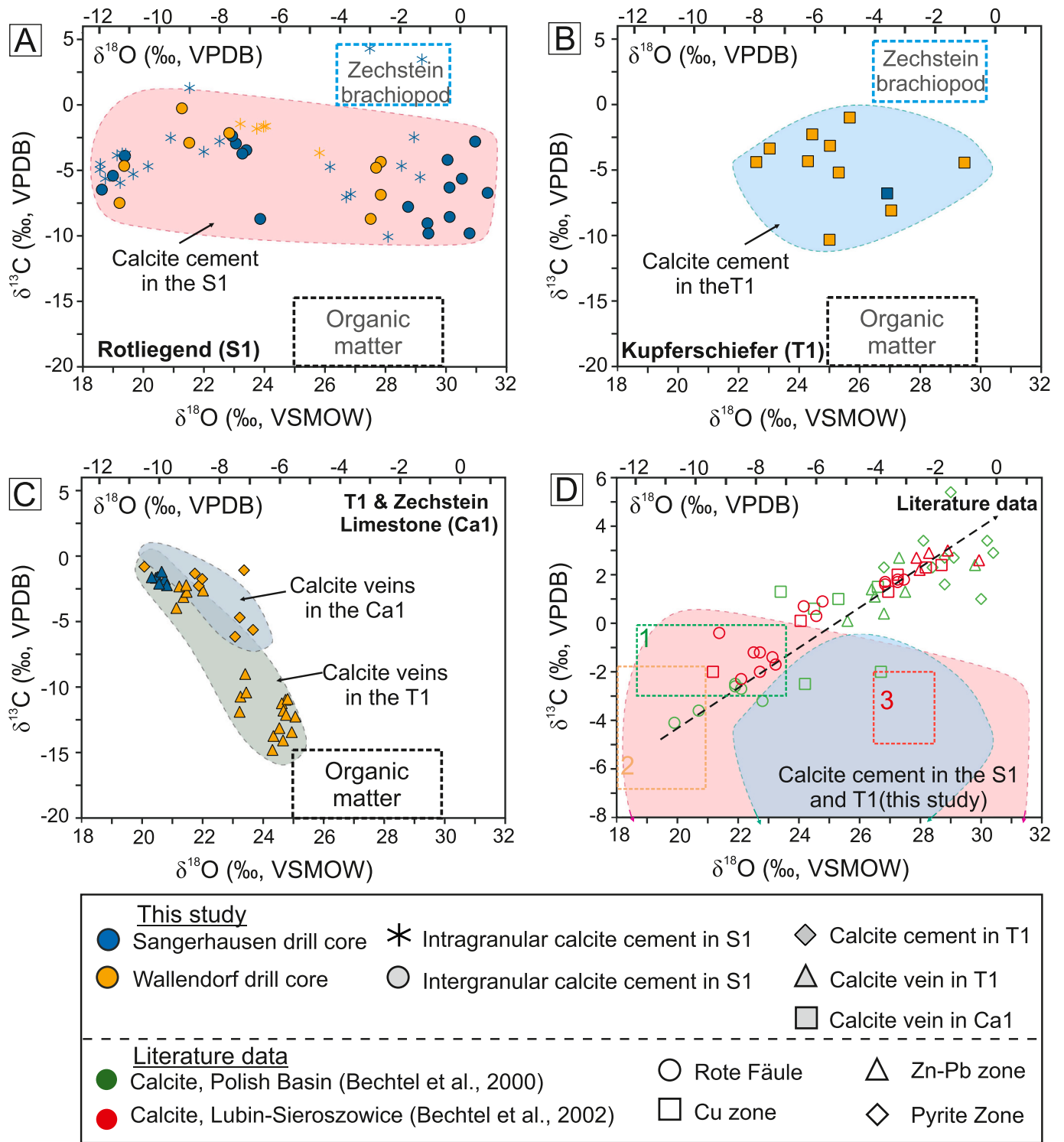


Fig. 11. Plot of $\delta^{18}\text{O}$ (‰, VSMOW or VPDB) vs $\delta^{13}\text{C}$ (‰, VPDB) values of calcite cement in samples from the (A) Rotliegend sandstone (S1) and (B) Kupferschiefer (T1), and (C) calcite veins in samples from the T1 and Zechstein Limestone (Ca1) from the Sangerhausen and Wallendorf drill cores. Only paired $\delta^{13}\text{C}$ and $\delta^{18}\text{O}$ values are plotted here, refer to Mohammedyasin et al. (2023b) for the full dataset. The $\delta^{13}\text{C}$ and $\delta^{18}\text{O}$ values for the Zechstein brachiopods from Germany and Poland are from Korte et al. (2005), while for those organic matter ($\delta^{13}\text{C} = -30\text{‰}$ to -15‰ , $\delta^{18}\text{O} = 24\text{‰}$ to 30‰) are from Hoefs (2019). (D) Comparison between $\delta^{13}\text{C}$ and $\delta^{18}\text{O}$ values of bulk carbonate (Bechtel et al. (2000, 2002) and in situ analyses in calcite cement from the S1 and T1 units in this study. The other literature data includes (1) calcite in the Rotliegend sandstone in the northern margin of the Central European Basin System ($\delta^{13}\text{C} = 0.5\text{‰}$ to -3‰ and $\delta^{18}\text{O} = -7\text{‰}$ to -12‰ , both in VPDB, Schöner and Gaupp, 2005), (2) calcite in the Rotliegend sandstone in north Germany ($\delta^{13}\text{C} = -6.7\text{‰}$ to -1.8‰ and $\delta^{18}\text{O} = -13.4\text{‰}$ to -9.7‰ , both in VPDB; Platt, 1994) and (3) calcite cement in condensed basal Zechstein limestone (Paproc 28) from western Poland ($\delta^{13}\text{C} = -4.5\text{‰}$ to -1.9‰ , and $\delta^{18}\text{O} = -4.1\text{‰}$ to -2.1‰ , both in VPDB; Peryt et al., 2015). Fig. D is plotted 1:1 to show the isotopic covariation trend of Bechtel et al. (2000, 2002).

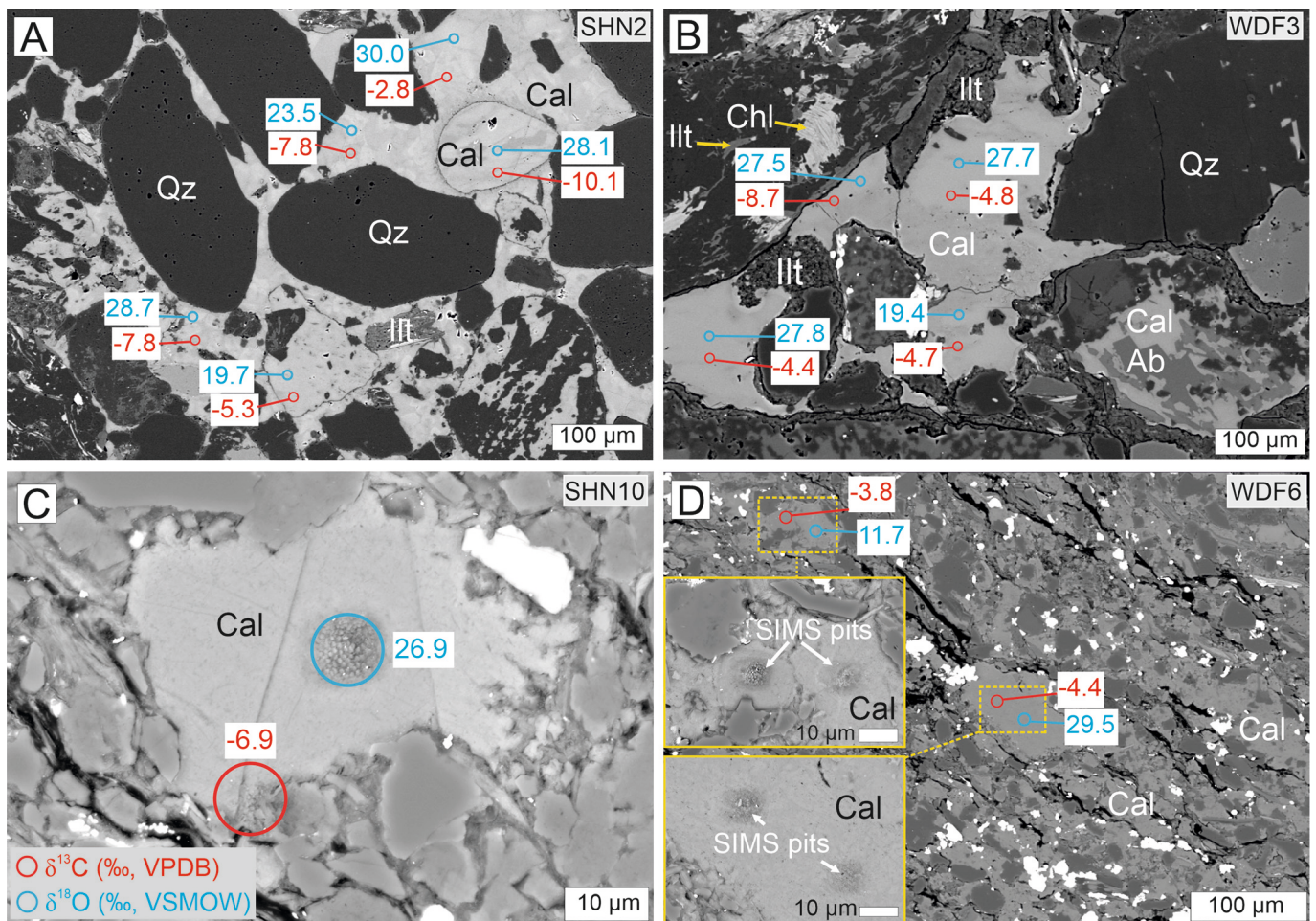


Fig. 12. BSE images with SIMS analysis-pit locations (circles) annotated with the respective $\delta^{13}\text{C}$ (‰, VPDB) and $\delta^{18}\text{O}$ (‰, VSMOW) values in calcite cement in the S1 (A, B) and T1 (C, D) samples from the Sangerhausen (SHN) and Wallendorf (WDF) drill cores. The inset BSE images in D shows SIMS analysis pits ($\sim 10\ \mu\text{m}$ in diameter). Note sample names on the top right of each image. Abbreviations: Ab = albite, Cal = calcite, Chl = chlorite, Ill = illite, Qz = quartz.

the studied samples, it is worth mentioning that there is no significant difference in the $\delta^{13}\text{C}$ and $\delta^{18}\text{O}$ values of calcite cement between samples with the Rote Fäule in the Sangerhausen drill core and without it in the Wallendorf drill core. This means it is difficult to associate the isotopic values of the calcite vein from the Sangerhausen drill core with the Rote Fäule alteration. Both unmineralized and mineralized calcite veins in the Wallendorf drill core preserve a wide range of $\delta^{13}\text{C}$ values (-14.8‰ to -1.4‰). The cause for this isotopic variability in calcite veins is not clear. One possible explanation is the variability in rates of organic matter degradation. For example, low rates of organic matter degradation result in higher carbon isotope variability in the precipitating calcite (Mozley and Burns, 1993).

5.3.2. Controls on oxygen isotope composition of calcite cement and veins

A wide range of processes and fluid reservoirs can influence the $\delta^{18}\text{O}$ values of carbonates in sedimentary basins. The oxygen isotopic composition of marine carbonate cement is largely controlled by the isotopic composition of pore fluids and precipitation temperature (Dietzel et al., 2009; Mozley and Burns, 1993). The precipitation temperatures of carbonate cement are commonly calculated using mineral-water equilibrium fractionation factors based on estimations of pore fluid $\delta^{18}\text{O}$ values and measured $\delta^{18}\text{O}$ values of the carbonate cement (e.g., Fayek et al., 2001; Śliwiński et al., 2016; Sun et al., 2021). Here, we use the calcite-water equilibrium fractionation of O'Neil et al. (1969) to calculate the precipitation temperature of calcite cement in the S1 and T1 units. To test the temperature control on the oxygen isotope

fractionation in the presented dataset, we assume that the oxygen isotopic composition of the pore fluids was dominantly influenced by the Zechstein seawater, which had a $\delta^{18}\text{O}$ value inferred from the Zechstein brachiopods in Germany and Poland (-1.2‰ to 2.5‰ , Korte et al., 2005). With the above constraints, the precipitation temperatures of calcite cement in the S1 and T1 are calculated at lower (-1.2‰ , scenario 1) and higher (2.5‰ , scenario 2) $\delta^{18}\text{O}$ values of the Zechstein brachiopods from the Zechstein Limestone in Germany and Poland (Korte et al., 2005).

Scenario 1: Initial pore-fluid composition for marine transgressive mudstones (T1) and underlying sandstones (S1) likely to be dominated by Zechstein seawater at the earliest stages of diagenesis. Therefore, we assume (1) the lower $\delta^{18}\text{O}$ value (-1.2‰) of the Zechstein brachiopods (Korte et al., 2005) could represent the unaltered pore fluids derived from the Zechstein seawater and (2) the highest (31‰ for both units) $\delta^{18}\text{O}$ value of calcite cement represents the earliest formed calcite cement at the lowest temperature. This gives the minimum calculated temperature for calcite cement in the S1 and T1 samples as low as $9\ ^\circ\text{C}$ (see Fig. 14). This temperature is slightly lower than the calculated precipitation temperature ($16\ ^\circ\text{C}$ at 29.2‰ for sample SHN2 and $26\ ^\circ\text{C}$ at 27.5 for sample SHN7) of calcite cement with positive $\delta^{13}\text{C}$ values, which have similar isotopic values to the Zechstein seawater. These temperatures in general suggest calcite cementation starts, near the sediment-water interface, soon after sediment deposition (Brodie et al., 2018; Fayek et al., 2001). This is consistent with the preservation of intergranular, early diagenetic, poikilotopic calcite cement that formed

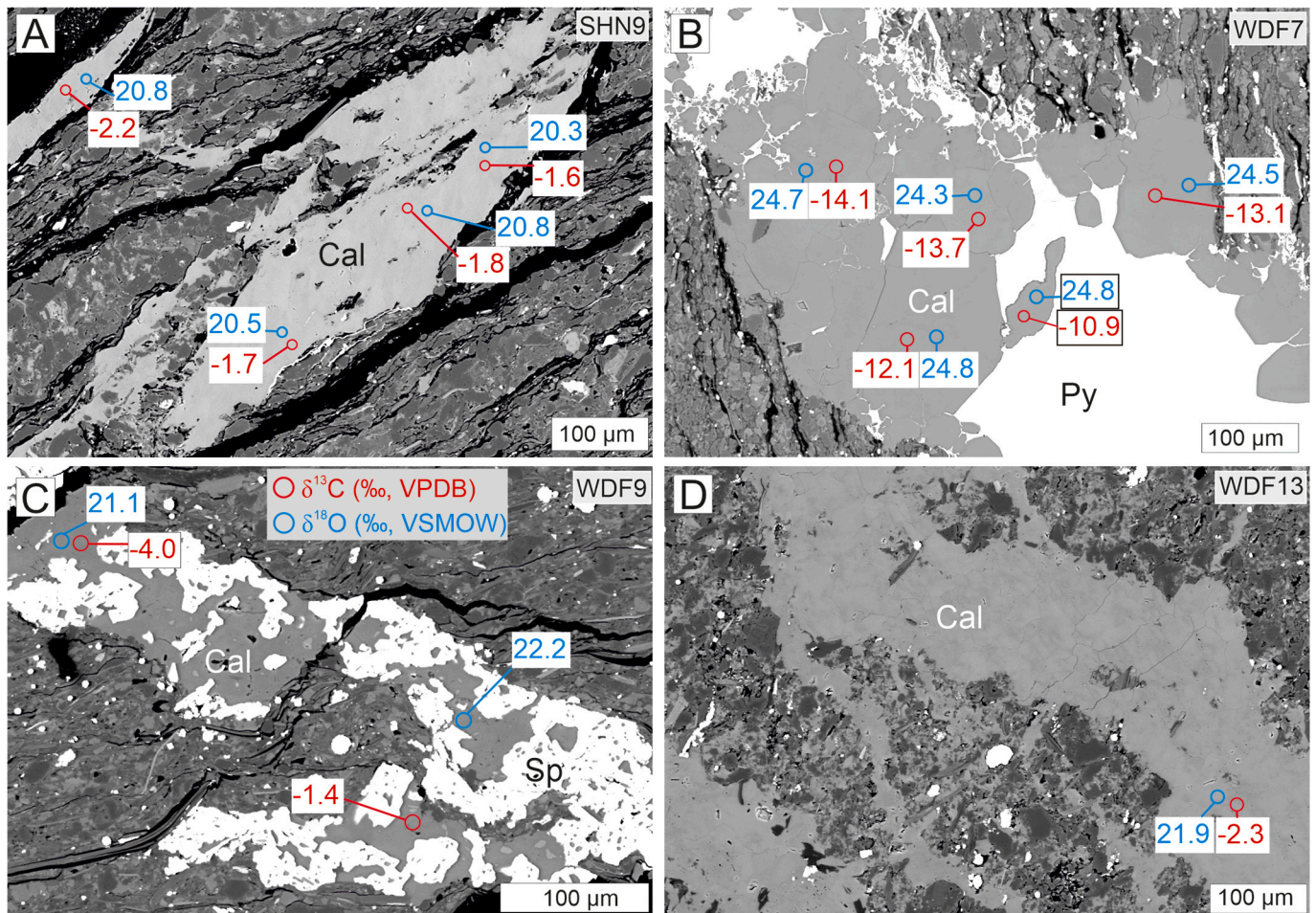


Fig. 13. The distribution of $\delta^{13}\text{C}$ (‰, VPDB) and $\delta^{18}\text{O}$ (‰, VSMOW) values in calcite veins in samples from the T1 in the Sangerhausen (A) and Wallendorf drill (B, C) cores, and (D) Cal in the Wallendorf drill core. Abbreviations: Cal = calcite, Py = pyrite, Sp = sphalerite.

at shallower depths before significant compaction (Mohammedyasin et al., 2023a). The high intergranular volume that has been occupied by calcite cement suggests that the calcite cement precipitation started during the earliest stages, as shown by several studies (e.g., Brodie et al., 2018; Fayek et al., 2001; Taylor et al., 2000).

Scenario 2: The second scenario assumes that the $\delta^{18}\text{O}$ value of the pore fluid has progressively evolved from the starting value of -1.2‰ (scenario 1) due to seawater evaporation. The high $\delta^{18}\text{O}$ value (up to 2.5‰) in the Zechstein brachiopods has been attributed to the high evaporation rates of the Zechstein seawater (Korte et al., 2005). Additionally, this scenario assumes that the lowest $\delta^{18}\text{O}$ values of calcite cement in the S1 (19‰) and T1 (22‰) represents precipitation at higher temperatures, which is more favorable for seawater evaporation. The patchy intergranular anhydrite that is coeval with calcite cement likely precipitated from an evaporative fluid in the Saale subbasin (Mohammedyasin et al., 2023a). In samples from the Spremberg subbasin (eastern Germany), the strong enrichment of deuterium in *n*-alkanes (up to -36‰) and isoprenoids (up to -20‰) also showed hydrogen exchange with an evaporitic fluid at temperatures $<110\text{ °C}$ (Poetz et al., 2022). Notably, the maximum calculated temperatures for calcite cement in the S1 (106 °C , $\delta^{18}\text{O}$ calcite = 19‰) and T1 (80 °C , $\delta^{18}\text{O}$ calcite = 22‰) are lower than the suggested temperature for mineralizing fluids from the Spremberg subbasin ($\sim 110\text{ °C}$, Poetz et al., 2022) and the Polish Kupferschiefer districts ($100\text{--}120\text{ °C}$, Bechtel et al., 2001, 2002; Bechtel and Püttmann, 1991).

The calculated temperatures from the two end-members have wider ranges ($9\text{--}106\text{ °C}$ in the S1 and $9\text{--}80\text{ °C}$ in the T1) compared to previous

studies in the S1 and T1 (e.g., Peryt et al., 2015; Platt, 1994). For example, Peryt et al. (2015) found a precipitation temperature of $23\text{--}34\text{ °C}$ for calcite in the T1 from western Poland assuming pore fluids $\delta^{18}\text{O}$ value similar to pristine modern seawater (0‰). The large range of calculated temperatures together with the lack of any specific isotopic trend in calcite cement in the studied samples do not represent a temperature-controlled system. This can be further supported by the lack of systematic covariation between $\delta^{13}\text{C}$ and $\delta^{18}\text{O}$ values of calcite cement in the Rote Fäule and across the different sulfide zones. Instead, the microscale isotopic variability provides evidence that pore-scale factors may have exerted a stronger control on the $\delta^{18}\text{O}$ values that are preserved by the calcite cement (Bojanowski et al., 2015).

The pore fluid chemistry across major sequence boundaries will be influenced by a number of factors, including seawater chemistry, meteoric water mixing, evaporative fluids, and diagenetic fluids derived from fluid-rock interaction, all of which can influence the $\delta^{18}\text{O}$ values preserved by calcite cements (Bojanowski, 2014; Mozley and Burns, 1993). The higher $\delta^{18}\text{O}$ values in calcite cement could be derived from evaporative fluids (Dreybrodt and Deininger, 2014; Horton et al., 2016), clay mineral diagenesis (e.g., Wilkinson et al., 1992) and hydrothermal brines (Reis et al., 2019; Śliwiński et al., 2016). The higher $\delta^{18}\text{O}$ values (up to 38.7‰ with $\delta^{13}\text{C}$ value of 3.7‰ , sample SHN4) of calcite cement, together with petrographic evidence that show coeval pore-filling anhydrite cement with calcite cement in the S1 (Mohammedyasin et al., 2023a), could reflect the influence of evaporated Zechstein seawater during its precipitation or burial diagenesis. The higher $\delta^{18}\text{O}$ values of calcite cement in the S1 and T1 are nearly similar to those of

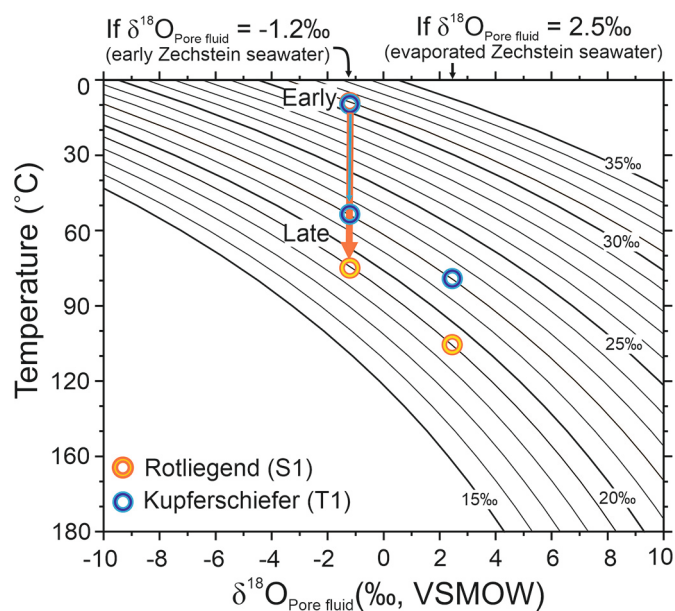


Fig. 14. Plot relating measured $\delta^{18}\text{O}$ values of calcite cement to the temperature of precipitation as a function of different pore fluid $\delta^{18}\text{O}$ values using calcite-water equilibrium fractionation factor of O'Neil et al. (1969). The sub-parallel lines stretching across the plot are $\delta^{18}\text{O}$ isopleths, representing constant $\delta^{18}\text{O}$ values (‰, VSMOW) of calcite cement. The $\delta^{18}\text{O}$ values of the calcite cement in the S1 samples progressively evolve from approximately 31‰ to 19‰ while in the T1 samples progressively evolve from approximately 31‰ to 22‰. The lower and higher $\delta^{18}\text{O}$ values of the Zechstein brachiopods ($\delta^{18}\text{O}_{\text{Pore fluid}} = -1.2\text{‰}$ to 2.5‰) in the Zechstein Limestone from Germany and Poland (Korte et al., 2005) were considered representative of early and evaporated Zechstein seawater, respectively.

the higher $\delta^{18}\text{O}$ values (up to 2.6‰ , VPDB) in the Zechstein brachiopods and have been attributed to the evaporation effect (Korte et al., 2005).

The decrease in the $\delta^{18}\text{O}$ values in the Rote Fäule from the Sangerhausen mining district has been linked to the inflow of meteoric groundwaters with low $\delta^{18}\text{O}$ values ascending from the Rotliegende sandstone (Hammer et al., 1990). The meteoric water may have derived from residual meteoric water within the Rotliegende (before the deposition of the T1), from the influx of meteoric water along erosional surfaces associated with paleohighs, or penetration along major faults in basin margin settings. The low $\delta^{18}\text{O}$ values in calcite from the Rotliegende sandstone in northern Germany have also been attributed to the influence of meteoric water from the basin margins during shallow burial, which is typical of carbonates precipitated in a playa lake environment (Platt, 1994). Similarly, the low $\delta^{18}\text{O}$ values in calcite cement in the studied S1 samples from the Sangerhausen and Wallendorf drill cores could indicate an influx of meteoric water. Some diagenetic alteration phases (e.g., kaolinite) have also been linked with meteoric water input in these samples (see Mohammedyasin et al., 2023a). Importantly, the host rock contribution, particularly the diagenetic alteration of volcanic rock fragments, could have resulted in lower $\delta^{18}\text{O}$ values in calcite cement. For instance, in the S1, in-situ alteration of mafic volcanic rock fragments mostly predates the extensive porosity occluding calcite cement (Mohammedyasin et al., 2023a).

5.4. Implications

The Cu and Pb–Zn mineralized rocks in the Allstedt, Wallendorf and Sangerhausen drill cores formed via the replacement of diagenetic carbonate (Mohammedyasin et al., 2023a). In other types of carbonate-replacement deposits (Carlin-type Au, intrusion-related Manto Zn), the surrounding host rocks commonly preserve km-scale isotopic alteration haloes as a result of fluid-rock interaction at elevated temperatures (e.g.,

175–250 °C, Arehart, 1996; Hofstra and Cline, 2000; 250–500 °C, Beinlich et al., 2019). Indeed, previous studies in the Kupferschiefer district have suggested that covariation between the $\delta^{13}\text{C}$ and $\delta^{18}\text{O}$ values in carbonate in the S1 and T1 units was caused by a temperature gradient (Fig. 11D), with the lowest $\delta^{18}\text{O}$ values in the Rote Fäule interpreted as an isotopic exchange between carbonate and isotopically distinct oxidizing mineralizing fluids (Bechtel et al., 2000, 2002). However, comparably low $\delta^{18}\text{O}$ values have also been reported in calcite from the Rotliegende sandstone in northern Germany, where they have been attributed to the influence of meteoric water from the basin margins during shallow burial (Platt, 1994).

Differentiating isotopic haloes that are derived from hydrothermal input from those derived from background processes (authigenic, diagenetic) is a major challenge in several mineral deposit systems (Frieauf and Pareja, 1998; Hickey et al., 2014; Stenger et al., 1998). Host rocks need to be subjected to high water/rock ratios (> 3) across a temperature gradient for the development of widespread isotopic haloes, which typically develop around systems with a large flux of reactive hydrothermal fluids through permeable host rocks (Beinlich et al., 2019; Stenger et al., 1998; Vazquez et al., 1998). The lack of systematic variability in the $\delta^{18}\text{O}$ values of calcite in the three drill cores indicates the temperature gradient and hydrothermal fluid flux (water/rock ratios) were not high enough to overprint and homogenize these background sources of isotopic variability. The maximum temperature estimates in the Sangerhausen mining district based on the maturation of organic matter (vitrinite reflectance values) are approximately 130 °C (Sun and Püttmann, 1997), which is further supported by recent constraints in the Spremberg subbasin (Poetz et al., 2022). In such low-temperature systems, the generation of an oxygen isotope halo in carbonates will largely be a function of the hydrothermal fluid flux and fluid flow pathways (Barker et al., 2013). The hydrothermal fluid flux would also have provided an overarching control on the size of the deposits in the Saale subbasin, which are relatively small compared to SSC deposits elsewhere in the SPB (e.g., Lubin-Sierszowice mining district, SW Poland). In the Sangerhausen district, local variability in the hydrothermal fluid flux may help to explain discrepancies with previous studies (cf. Bechtel et al., 2002). In the samples investigated here, the lack of an isotopic halo may indicate that the hydrothermal flux was insufficient to overprint the background variability. Future studies should therefore focus on whether isotopic haloes are resolvable around larger SSC deposits in the Kupferschiefer district.

6. Conclusions

The southern margin of the Southern Permian Basin (SPB) in Central Europe is well-known for SSC mineralization hosted in carbonaceous host rocks. In the Saale subbasin, the Kupferschiefer system that includes the uppermost part of the Rotliegende sandstone (S1), Kupferschiefer (T1), and lowermost part of the Zechstein Limestone (Ca1), has a significant proportion of diagenetic carbonate cement. A detailed cathodoluminescence (CL) characterization of calcite cement in the S1, T1 and Ca1 showed a similar, CL luminescent calcite cement. The high-spatial resolution in situ carbon and oxygen isotope analysis of the calcite cement in the S1 and T1 units from different drill cores showed a wide range of isotopic values ($> 10\text{‰}$) and microscale variabilities in calcite cement. The similar CL response, major element chemistry, and overlapping $\delta^{13}\text{C}$ and $\delta^{18}\text{O}$ values in calcite cement in samples from both units indicate that calcite cement was derived from fluids of similar composition. The $\delta^{13}\text{C}$ values (S1 = -10.1‰ to 4.3‰ , T1 = -12.9‰ to -0.3‰) of calcite cement indicate sources of alkalinity for the calcite cement derived from seawater-derived fluids and organic matter degradation. The calcite veins have relatively more negative $\delta^{13}\text{C}$ values (-14.8‰ to -1.4‰) that indicate carbonate alkalinity derived from the oxidation of organic matter in the T1. The lack of systematic covariation between $\delta^{13}\text{C}$ and $\delta^{18}\text{O}$ values of calcite cement, together with the isotopic variabilities at the microscale and the similarities in isotopic values

in the Rote Fäule and different sulfide zones, indicate the $\delta^{18}\text{O}$ values in calcite cement were dominantly influenced by variable pore fluid compositions, not by temperature. The higher $\delta^{18}\text{O}$ values of calcite cement could reflect a very minimal influence of evaporated Zechstein seawater. The lower $\delta^{18}\text{O}$ values in calcite cement suggest oxygen isotopes influenced by the diagenetic alteration of detrital clasts as shown by widespread in situ alteration of mafic volcanic rock fragments with a minor contribution from meteoric water. The lack of systematic isotopic variability in the calcite cement of the studied samples indicates the mineralizing fluid flux or temperature was insufficient to overprint the background sources of isotopic variability. This may also help to explain the modest size of SSC deposits in this part of the Kupferschiefer district.

Declaration of Competing Interest

The authors declare that they have no known competing financial interests or personal relationships that could have appeared to influence the work reported in this paper.

Acknowledgements

Funding for this project was provided by the Helmholtz Recruitment Initiative grant to Sarah Gleeson. We acknowledge the Landesamt für Geologie und Bergwesen, Sachsen-Anhalt for supplying core samples from their repository. We thank U. Dittmann for thin- and thick-sections preparation, I. Schäpan for SEM analysis and F. Couffignal for assistance in the SIMS lab, all at GFZ Potsdam. This work benefited from the insightful review of Christian Ihlenfeld.

Appendix A. Supplementary data

Supplementary data to this article can be found online at <https://doi.org/10.1016/j.chemgeo.2023.121811>.

References

- Allison, C.E., Francey, R.J., Meijer, H.A.J., 1995. Reference and intercomparison materials for stable isotopes of light elements. IAEA-TECD-825, 155–162.
- Arehart, G.B., 1996. Characteristics and origin of sediment-hosted disseminated gold deposits: a review. *Ore Geol. Rev.* 11, 383–403. [https://doi.org/10.1016/S0169-1368\(96\)00010-8](https://doi.org/10.1016/S0169-1368(96)00010-8).
- Baele, J.-M., Decrée, S., Rusk, B., 2019. Cathodoluminescence applied to ore geology and exploration. In: *Ore Deposits*, Geophysical Monograph Series, pp. 131–161. <https://doi.org/10.1002/9781119290544.ch6>.
- Baertschi, P., 1976. Absolute ^{18}O content of standard mean ocean water. *Earth Planet. Sci. Lett.* 31, 341–344. [https://doi.org/10.1016/0012-821X\(76\)90115-1](https://doi.org/10.1016/0012-821X(76)90115-1).
- Baldschuhn, R., Binot, F., Fleig, S., Kockel, F., 2001. *Geotektonischer Atlas von Nordwest-Deutschland und dem-deutschen Nordsee-Sektor*. Geol. Jahrb. R. A, Band A 153 15, 3–95.
- Barker, S.L.L., Dipple, G.M., 2019. Exploring for carbonate-hosted ore deposits using carbon and oxygen isotopes. In: *Ore Deposits: Origin, Exploration, and Exploitation*. Wiley Online Library, pp. 185–207. <https://doi.org/10.1002/9781119290544.ch8>.
- Barker, S.L.L., Dipple, G.M., Hickey, K.A., Lepore, W.A., Vaughan, J.R., 2013. Applying stable isotopes to mineral exploration: Teaching an old dog new tricks. *Econ. Geol.* 108, 1–9. <https://doi.org/10.2113/econgeo.108.1.1>.
- Bechtel, A., Püttmann, W., 1991. The origin of the Kupferschiefer-type mineralization in the Richelsdorf Hills, Germany, as deduced from stable isotope and organic geochemical studies. *Chem. Geol.* 91, 1–18. [https://doi.org/10.1016/0009-2541\(91\)90012-G](https://doi.org/10.1016/0009-2541(91)90012-G).
- Bechtel, A., Gratzner, R., Püttmann, W., Oszczepalski, S., 2000. Geochemical and isotopic composition of organic matter in the Kupferschiefer of the Polish Zechstein basin: relation to maturity and base metal mineralization. *Int. J. Earth Sci.* 89, 72–89. <https://doi.org/10.1007/s005310050318>.
- Bechtel, A., Sun, Y., Püttmann, W., Hoernes, S., Hoefs, J., 2001. Isotopic evidence for multi-stage base metal enrichment in the Kupferschiefer from the Sangerhausen Basin, Germany. *Chem. Geol.* 176, 31–49. [https://doi.org/10.1016/S0009-2541\(00\)00336-3](https://doi.org/10.1016/S0009-2541(00)00336-3).
- Bechtel, A., Gratzner, R., Püttmann, W., Oszczepalski, S., 2002. Geochemical characteristics across the oxic/anoxic interface (Rote Fäule front) within the Kupferschiefer of the Lubin-Sierosowice mining district (SW Poland). *Chem. Geol.* 185, 9–31. [https://doi.org/10.1016/S0009-2541\(01\)00395-3](https://doi.org/10.1016/S0009-2541(01)00395-3).
- Beinlich, A., Barker, S.L.L., Dipple, G.M., Hansen, L.D., Megaw, P.K.M., 2019. Large-scale stable isotope alteration around the hydrothermal carbonate-replacement Cinco de Mayo Zn-Ag Deposit, Mexico. *Econ. Geol.* 114, 375–396. <https://doi.org/10.5382/econgeo.2019.4635>.
- Bjørlykke, K., Jahren, J., 2012. Open or closed geochemical systems during diagenesis in sedimentary basins: Constraints on mass transfer during diagenesis and the prediction of porosity in sandstone and carbonate reservoirs. *Am. Assoc. Pet. Geol. Bull.* 96, 2193–2214. <https://doi.org/10.1306/04301211139>.
- Bojanowski, M.J., 2014. Authigenic dolomites in the Eocene–Oligocene organic carbon-rich shales from the Polish Outer Carpathians: Evidence of past gas production and possible gas hydrate formation in the Silesian basin. *Mar. Pet. Geol.* 51, 117–135. <https://doi.org/10.1016/j.marpetgeo.2013.12.001>.
- Bojanowski, M.J., Bagiński, B., Guillemer, C., Franchi, I.A., 2015. Carbon and oxygen isotope analysis of hydrate-associated Oligocene authigenic carbonates using NanoSIMS and IRMS. *Chem. Geol.* 416, 51–64. <https://doi.org/10.1016/j.chemgeo.2015.10.021>.
- Borg, G., Piestrzynski, A., Bachmann, G.H., Püttmann, W., Walther, S., Fiedler, M., 2012. An Overview of the European Kupferschiefer Deposits *. In: Hedenquist, J.W., Harris, M., Camus, F. (Eds.), *Geology and Genesis of Major Copper Deposits and Districts of the World: A Tribute to Richard H. Sillitoe*, Society of Economic Geologists, 16, pp. 455–486. <https://doi.org/10.5382/SP.16.18>.
- Breitkreuz, C., Geißler, M., Schneider, J., Kiersnowski, H., 2008. Basin initiation: volcanism and sedimentation. In: Littke, R., Bayer, U., Gajewski, D., Nelskamp, S. (Eds.), *Dynamics of Complex Intracontinental Basins*. Springer-Verlag, Berlin, pp. 173–180.
- Brodie, M.W., Aplin, A.C., Hart, B., Orland, I.J., Valley, J.W., Boyce, A.J., 2018. Oxygen isotope microanalysis by secondary ion mass spectrometry suggests continuous 300-million-year history of calcite cementation and dolomitization in the Devonian Bakken Formation. *J. Sediment. Res.* 88, 91–104. <https://doi.org/10.2110/jsr.2018.1>.
- Craig, H., 1957. Isotopic standards for carbon and oxygen and correction factors for mass-spectrometric analysis of carbon dioxide. *Geochim. Cosmochim. Acta* 12, 133–149. [https://doi.org/10.1016/0016-7037\(57\)90024-8](https://doi.org/10.1016/0016-7037(57)90024-8).
- Cui, H., Kitajima, K., Orland, I.J., Xiao, S., Baele, J.-M., Kaufman, A.J., Denny, A., Zhou, C., Spicuzza, M.J., Fournelle, J.H., 2021. Deposition or diagenesis? Probing the Ediacaran Shuram excursion in South China by SIMS. *Glob. Planet. Chang.* 206, 103591. <https://doi.org/10.1016/j.gloplacha.2021.103591>.
- Denny, A.C., Orland, I.J., Valley, J.W., 2020. Regionally correlated oxygen and carbon isotope zonation in diagenetic carbonates of the Bakken Formation. *Chem. Geol.* 531, 119327. <https://doi.org/10.1016/j.chemgeo.2019.119327>.
- Dietzel, M., Tang, J., Leis, A., Köhler, S.J., 2009. Oxygen isotopic fractionation during inorganic calcite precipitation—Effects of temperature, precipitation rate and pH. *Chem. Geol.* 268, 107–115. <https://doi.org/10.1016/j.chemgeo.2009.07.015>.
- Dreybrodt, W., Deininger, M., 2014. The impact of evaporation to the isotope composition of DIC in calcite precipitating water films in equilibrium and kinetic fractionation models. *Geochim. Cosmochim. Acta* 125, 433–439. <https://doi.org/10.1016/j.gca.2013.10.004>.
- Ehrenberg, S.N., Walderhaug, O., Bjørlykke, K., 2012. Carbonate porosity creation by mesogenic dissolution: reality or illusion? *Am. Assoc. Pet. Geol. Bull.* 96, 217–233. <https://doi.org/10.1306/05031110187>.
- Erzberger, R., Franz, R., Jung, W., Knitzschke, G., Langer, M., Luge, J., Rentzsch, H., Rentzsch, J., 1968. *Lithologie, paläogeographie und metallführung des kupferschiefers in der Deutschen Demokratischen Republik*. Geologie 17, 776–791.
- Fayek, M., Harrison, T.M., Grove, M., McKeegan, K.D., Coath, C.D., Boles, J.R., 2001. In situ stable isotopic evidence for protracted and complex carbonate cementation in a petroleum reservoir, North Coles Levee, San Joaquin Basin, California, USA. *J. Sediment. Res.* 71, 444–458. <https://doi.org/10.1306/2DC40954-0E47-11D7-8643000102C1865D>.
- Friehauf, K.C., Pareja, G.A., 1998. Can oxygen isotope halos be produced around high-temperature dolostone-hosted ore deposits? Evidence from the Superior district, Arizona. *Econ. Geol.* 93, 639–650. <https://doi.org/10.2113/gsecongeo.93.5.639>.
- Gaitzsch, B., 1995. *Grüneberg-Formation*, in: *Stratigraphie von Deutschland I: Norddeutsches Rotliegendebcken - Rotliegend- Monographie Teil II*. Cour Forsch-Inst Senckenberg 183, 102–106.
- Geologisches Landesamt Sachsen-Anhalt, 1993. *Geologische Übersichtskarte von Sachsen-Anhalt 1:400,000*. Geologisches Landesamt Sachsen-Anhalt, Halle, Germany.
- Geologisches Landesamt Sachsen-Anhalt, 2000. *Geologisch-Montanhistorische Karte der reviere Mansfeld und Sangerhausen 1:50,000*. Geologisches Landesamt Sachsen-Anhalt, Halle, Germany.
- Giles, M.R., 1987. Mass transfer and problems of secondary porosity creation in deeply buried hydrocarbon reservoirs. *Mar. Pet. Geol.* 4, 188–204. [https://doi.org/10.1016/0264-8172\(87\)90044-4](https://doi.org/10.1016/0264-8172(87)90044-4).
- Glennie, K.W., Buller, A.T., 1983. The Permian Weisliedend of NW Europe: the partial deformation of aeolian dune sands caused by the Zechstein transgression. *Sediment. Geol.* 35, 43–81. [https://doi.org/10.1016/0037-0738\(83\)90069-6](https://doi.org/10.1016/0037-0738(83)90069-6).
- Götze, J., Schertl, H.-P., Neuser, R.D., Kempe, U., Hanchar, J.M., 2013. Optical microscope-cathodoluminescence (OM-CL) imaging as a powerful tool to reveal internal textures of minerals. *Mineral. Petrol.* 107, 373–392. <https://doi.org/10.1007/s00710-012-0256-0>.
- Hammer, J., Junge, F., Rösler, H.J., Niese, S., Gleisberg, B., Stiehl, G., 1990. Element and isotope geochemical investigations of the Kupferschiefer in the vicinity of "Rote Fäule", indicating copper mineralization (Sangerhausen basin, GDR). *Chem. Geol.* 85, 345–360. [https://doi.org/10.1016/0009-2541\(90\)90012-V](https://doi.org/10.1016/0009-2541(90)90012-V).
- Hickey, K.A., Ahmed, A.D., Barker, S.L.L., Leonardson, R., 2014. Fault-controlled lateral fluid flow underneath and into a Carlin-type gold deposit: isotopic and geochemical footprints. *Econ. Geol.* 109, 1431–1460. <https://doi.org/10.2113/econgeo.109.5.1431>.
- Hitzman, M., Kirkham, R., Broughton, D., Thorson, J., Selley, D., 2005. The sediment-hosted stratiform copper ore system. In: Hedenquist, J.W., Thompson, J.F.H.,

- Goldfarb, R.J., Richards, J.P. (Eds.), One Hundredth Anniversary Volume. Society of Economic Geologists, pp. 609–642. <https://doi.org/10.5382/AV100.19>.
- Hoefs, J., 2019. Stable Isotope Geochemistry, 8th ed. Springer Cham. <https://doi.org/10.1007/978-3-319-78527-1>.
- Hofstra, A.H., Cline, J.S., 2000. Characteristics and models for Carlin-type gold deposits. In: Steffen, G., Hagemann, P.E.B. (Eds.), Gold in, 2000, pp. 163–220. <https://doi.org/10.5382/Rev.13.05>.
- Horton, T.W., Defliese, W.F., Tripathi, A.K., Oze, C., 2016. Evaporation induced 18O and 13C enrichment in lake systems: a global perspective on hydrologic balance effects. *Quat. Sci. Rev.* 131, 365–379. <https://doi.org/10.1016/j.quascirev.2015.06.030>.
- IAEA, 2016. Reference Sheet for IAEA-603.
- Kaiser, R., Nöth, S., Ricken, W., 2003. Sequence stratigraphy with emphasis on platform-related parasequences of the Zechstein 2 carbonate (Ca2)–the northern platform margin of the Southern Permian Basin (NE Germany). *Int. J. Earth Sci.* 92, 54–67. <https://doi.org/10.1007/s00531-002-0292-9>.
- Kelley, K.D., Dumoulin, J.A., Jennings, S., 2004. The Anarraaq Zn-Pb-Ag and barite deposit, northern Alaska: evidence for replacement of carbonate by barite and sulfides. *Econ. Geol.* 99, 1577–1591. <https://doi.org/10.2113/gsecongeo.99.7.1577>.
- Kita, N.T., Ushikubo, T., Fu, B., Valley, J.W., 2009. High precision SIMS oxygen isotope analysis and the effect of sample topography. *Chem. Geol.* 264, 43–57. <https://doi.org/10.1016/j.chemgeo.2009.02.012>.
- Korte, C., Jasper, T., Kozur, H.W., Veizer, J., 2005. $\delta^{18}\text{O}$ and $\delta^{13}\text{C}$ of Permian brachiopods: a record of seawater evolution and continental glaciation. *Palaeogeogr. Palaeoclimatol. Palaeoecol.* 224, 333–351. <https://doi.org/10.1016/j.palaeo.2005.03.015>.
- Kozdon, R., Ushikubo, T., Kita, N.T., Spicuzza, M., Valley, J.W., 2009. Intratrust oxygen isotope variability in the planktonic foraminifer *N. pachyderma*: real vs. apparent vital effects by ion microprobe. *Chem. Geol.* 258, 327–337. <https://doi.org/10.1016/j.chemgeo.2008.10.032>.
- Kulick, J., Leifeld, D., Meisl, S., Pöschl, W., Stellmacher, R., Strecker, G., 1984. Petrofazielle und chemische Erkundung des Kupferschiefers der Hessischen Senke und des Harz-Westrandes. *Geol. Jahrbuch. R. D. Mineral. Petrogr. Geochemie, Lagerstättenkd.* D68, 3–223.
- Legler, B., Gebhardt, U., Schneider, J.W., 2005. Late Permian non-marine-marine transitional profiles in the central Southern Permian Basin, northern Germany. *Int. J. Earth Sci.* 94, 851–862. <https://doi.org/10.1007/s00531-005-0002-5>.
- Machel, H.G., Burton, E.A., 1991. Factors governing cathodoluminescence in calcite and dolomite, and their implications for studies of carbonate diagenesis. *SEPM Short Course Notes* 25, 37–57. <https://doi.org/10.2110/scn.91.25.0037>.
- Marshall, J.D., 1988. Cathodoluminescence of Geological Materials. Unwin Hyman Ltd.
- Maystrenko, Y., Bayer, U., Brink, H.-J., Littke, R., 2008. The Central European Basin System - an Overview. In: Littke, R., Bayer, U., Gajewski, D., Nelskamp, S. (Eds.), Dynamics of Complex Intracontinental Basins - The Central European Basin System. Springer-Verlag, Berlin Heidelberg, Berlin, pp. 17–34.
- Mohammadyasin, M.S., Magnall, J.M., Gleeson, S.A., Schulz, H.-M., Schleicher, A.M., Stammeier, J.A., Ehling, B.-C., 2023a. Diagenetic history and timing of Cu and Zn-Pb sulfide mineralization in the Permian Kupferschiefer system, Saale subbasin, eastern Germany. *Econ. Geol.* 118, 1467–1494. <https://doi.org/10.5382/econgeo.5015>.
- Mohammadyasin, M.S., Magnall, J.M., Gleeson, S.A., Schulz, H.-M., Scicchitano, M.R., 2023c. Carbon and oxygen isotope in situ analysis of calcite using secondary ion mass spectrometry in the Permian Kupferschiefer system of the Saale subbasin, eastern Germany. *GFZ Data Serv.* <https://doi.org/10.5880/GFZ.3.1.2023.003>.
- Morad, S., Ketzler, J.M., De Ros, L.F., 2000. Spatial and temporal distribution of diagenetic alterations in siliciclastic rocks: implications for mass transfer in sedimentary basins. *Sedimentology* 47, 95–120. <https://doi.org/10.1046/j.1365-3091.2000.00007.x>.
- Mozley, P.S., Burns, S.J., 1993. Oxygen and carbon isotopic composition of marine carbonate concretions; an overview. *J. Sediment. Res.* 63, 73–83. <https://doi.org/10.1306/D4267A91-2B26-11D7-8648000102C1865D>.
- O’Neil, J.R., Clayton, R.N., Mayeda, T.K., 1969. Oxygen isotope fractionation in divalent metal carbonates. *J. Chem. Phys.* 51, 5547–5558. <https://doi.org/10.1063/1.1671982>.
- Oszczepalski, S., 1999. Origin of the Kupferschiefer polymetallic mineralization in Poland. *Mineral. Deposita* 34, 599–613. <https://doi.org/10.1007/s001260050222>.
- Oszczepalski, S., Speczik, S., Zieliński, K., Chmielewski, A., 2019. The Kupferschiefer deposits and prospects in SW Poland: past, present and future. *Minerals* 9, 1–42. <https://doi.org/10.3390/min9100592>.
- Paul, J., 2006. Der Kupferschiefer: Lithologie, Stratigraphie, Fazies und Metallogenese eines Schwarzschiefers. *Zeitschrift der Dtsch. Gesellschaft für Geowissenschaften* 157, 57–76. <https://doi.org/10.1127/1860-1804/2006/0157-0057>.
- Peryt, T.M., Halas, S., Peryt, D., 2015. Carbon and oxygen isotopic composition and foraminifers of condensed Zechstein (Upper Permian) strata in western Poland: environmental and stratigraphic implications. *Geol. J.* 50, 446–464. <https://doi.org/10.1002/gj.2549>.
- Pharaoh, T., Dusar, M., Geluk, M., Kockel, F., Krawczyk, C., Krzywiec, P., Scheck-Wenderoth, M., Thybo, H., Vejbaek, O., van Wees, J.D., 2010. Chapter 3-Tectonic evolution. In: Doornbal, H., Stevenson, A. (Eds.), Petroleum Geological Atlas of the Southern Permian Basin Area. European Association of Geoscientists and Engineers Publications b.v. Houten, The Netherlands, pp. 25–57.
- Pieczonka, J., Piestrzyński, A., Mucha, J., Gluszek, A., Kotarba, M.J., Węclaw, D., 2008. The red-bed-type precious metal deposit in the Sieroszewice-Polkowice copper mining district, SW Poland. *Ann. Soc. Geol. Pol.* 78, 151–280.
- Pierson, B.J., 1981. The control of cathodoluminescence in dolomite by iron and manganese. *Sedimentology* 28, 601–610. <https://doi.org/10.1111/j.1365-3091.1981.tb01924.x>.
- Piestrzyński, A., Pieczonka, J., Gluszek, A., 2002. Redbed-type gold mineralisation, Kupferschiefer, south-west Poland. *Mineral. Deposita* 37, 512–528. <https://doi.org/10.1007/s00126-002-0256-9>.
- Pinet, N., Sack, P., Mercier-Langevin, P., Davis, W.J., Petts, D.C., Lavoie, D., Percival, J. B., Dubé, B., Colpron, M., Haeri-Ardakani, O., 2022. Yukon’s Carlin-type gold deposits (Rackla Belt, Canada): main characteristics and new insights on alteration styles and geochemistry. *Econ. Geol.* 117, 875–904. <https://doi.org/10.5382/econgeo.4899>.
- Platt, J.D., 1994. Geochemical evolution of pore waters in the Rotliegend (Early Permian) of northern Germany. *Mar. Pet. Geol.* 11, 66–78. [https://doi.org/10.1016/0264-8172\(94\)90010-8](https://doi.org/10.1016/0264-8172(94)90010-8).
- Plein, E., 1990. The southern Permian Basin and its paleogeography. In: Heling, D., Rothe, P., Förstner, U., Stoffers, P. (Eds.), Sediments and Environmental Geochemistry. Springer-Verlag, Berlin Heidelberg, Berlin, pp. 124–133.
- Poetz, S., Liu, Y., Magnall, J.M., Vieth-Hillebrand, A., Yang, S., Göthel, M., Gleeson, S.A., Schulz, H.-M., 2022. Signals of low grade organic matter alteration in the Upper Permian Kupferschiefer (Spremberg area, Eastern Germany)—a by-product of copper mineralization? *Org. Geochem.* 169, 104421. <https://doi.org/10.1016/j.orgchem.2022.104421>.
- Radzinski, K.-H., 2008. Zechstein. In: Bachmann, G.H., Ehling, B.-C., Eichner, R., Schwab, M. (Eds.), *Geologie von Sachsen-Anhalt*, pp. 160–178.
- Reis, A., Erhardt, A.M., McGlue, M.M., Waite, L., 2019. Evaluating the effects of diagenesis on the $\delta^{13}\text{C}$ and $\delta^{18}\text{O}$ compositions of carbonates in a mud-rich depositional environment: a case study from the Midland Basin, USA. *Chem. Geol.* 524, 196–212. <https://doi.org/10.1016/j.chemgeo.2019.06.021>.
- Ruebsam, W., Dickson, A.J., Hoyer, E.-M., Schwark, L., 2017. Multiproxy reconstruction of oceanographic conditions in the southern epeiric Kupferschiefer Sea (Late Permian) based on redox-sensitive trace elements, molybdenum isotopes and biomarkers. *Gondwana Res.* 44, 205–218. <https://doi.org/10.1016/j.gr.2016.10.017>.
- Schneider, J., Gebhardt, U., 1993. Litho- und Biofaziesmuster in intra- und extramontanen Senken des Rotliegend (Perm, Nord- und Ostdeutschland). *Geol. Jahrbuch. R. A* 131, 57–98.
- Schobben, M., Ullmann, C.V., Leda, L., Korn, D., Struck, U., Reimold, W.U., Ghaderi, A., Algeo, T.J., Korte, C., 2016. Discerning primary versus diagenetic signals in carbonate carbon and oxygen isotope records: An example from the Permian-Triassic boundary of Iran. *Chem. Geol.* 422, 94–107. <https://doi.org/10.1016/j.chemgeo.2015.12.013>.
- Schöner, R., Gaupp, R., 2005. Contrasting red bed diagenesis: the southern and northern margin of the Central European Basin. *Int. J. Earth Sci.* 94, 897–916. <https://doi.org/10.1007/s00531-005-0004-3>.
- Selley, D., Broughton, D., Scott, R., Hitzman, M., Bull, S., Large, R., McGoldrick, P., Croaker, M., Pollington, N., Barra, F., 2005. A new look at the geology of the Zambian Copperbelt. In: Hedenquist, J.W., Thompson, J.F.H., Goldfarb, R.J., Richards, J.P. (Eds.), One Hundredth Anniversary Volume. Society of Economic Geologists, pp. 609–642. <https://doi.org/10.5382/AV100.29>.
- Śliwiński, M.G., Kozdon, R., Kitajima, K., Denny, A., Valley, J.W., 2016. Microanalysis of carbonate cement $\delta^{18}\text{O}$ in a CO₂-storage system seal: Insights into the diagenetic history of the Eau Claire Formation (Upper Cambrian), Illinois Basin. *Am. Assoc. Pet. Geol. Bull.* 100, 1003–1031. <https://doi.org/10.1306/02031615065>.
- Spinks, S.C., Pearce, M.A., Liu, W., Kunzmann, M., Ryan, C.G., Moorhead, G.F., Kirkham, R., Blaikie, T., Sheldon, H.A., Schaub, P.M., 2021. Carbonate replacement as the principal Ore formation process in the Proterozoic McArthur River (HYC) Sediment-Hosted Zn-Pb Deposit, Australia. *Econ. Geol.* 116, 693–718. <https://doi.org/10.5382/econgeo.4793>.
- Stedingk, K., Rentsch, J., Knitzschke, G., Schenke, G., Heinrich, K., Scheffler, H., 2002. Potenziale der Erze und Spate in Sachsen-Anhalt. *Landesamt für Geologie und Bergwesen Sachsen-Anhalt Rohstoffbericht* 5, 75–131.
- Stenger, D.P., Kessler, S.E., Vennemann, T., 1998. Carbon and oxygen isotope zoning around Carlin-type gold deposits: a reconnaissance survey at Twin Creeks, Nevada. *J. Geochem. Explor.* 63, 105–121. [https://doi.org/10.1016/S0375-6742\(98\)00049-1](https://doi.org/10.1016/S0375-6742(98)00049-1).
- Stollhofen, H., Bachmann, G.H., Barnasch, J., Bayer, U., Beutler, G., Franz, M., Kästner, M., Legler, B., Mutterlose, J., Radies, D., 2008. Upper Rotliegend to Early Cretaceous basin development. In: Littke, R., Bayer, Ulf, Gajewski, D., Nelskamp, S. (Eds.), Dynamics of Complex Intracontinental Basins. Springer-Verlag, Berlin Heidelberg, pp. 181–210.
- Strohmer, C., Voigt, E., Zimdars, J., 1996. Sequence stratigraphy and cyclic development of Basal Zechstein carbonate-evaporite deposits with emphasis on Zechstein 2 off-platform carbonates (Upper Permian, Northeast Germany). *Sediment. Geol.* 102, 33–54. [https://doi.org/10.1016/0037-0738\(95\)00058-5](https://doi.org/10.1016/0037-0738(95)00058-5).
- Sun, Y., Püttmann, W., 1997. Metal accumulation during and after deposition of the Kupferschiefer from the Sangerhausen Basin, Germany. *Appl. Geochem.* 12, 577–592. [https://doi.org/10.1016/S0883-2927\(97\)00015-2](https://doi.org/10.1016/S0883-2927(97)00015-2).
- Sun, Y., Püttmann, W., 2000. The role of organic matter during copper enrichment in Kupferschiefer from the Sangerhausen basin, Germany. *Org. Geochem.* 31, 1143–1161. [https://doi.org/10.1016/S0146-6380\(00\)00117-0](https://doi.org/10.1016/S0146-6380(00)00117-0).
- Sun, F., Hu, W., Wu, H., Fu, B., Wang, X., Tang, Y., Cao, J., Yang, S., Hu, Z., 2021. Two-stage mineral dissolution and precipitation related to organic matter degradation: Insights from in situ C–O isotopes of zoned carbonate cements. *Mar. Pet. Geol.* 124, 104812. <https://doi.org/10.1016/j.marpetgeo.2020.104812>.
- Taylor, K.G., Gawthorpe, R.L., Curtis, C.D., Marshall, J.D., Awwiller, D.N., 2000. Carbonate cementation in a sequence-stratigraphic framework: Upper cretaceous sandstones, Book Cliffs, Utah-Colorado. *J. Sediment. Res.* 70, 360–372. <https://doi.org/10.1306/2DC40916-0E47-11D7-8643000102C1865D>.

- Tucker, M.E., 1991. Sequence stratigraphy of carbonate-evaporite basins: models and application to the Upper Permian (Zechstein) of northeast England and adjoining North Sea. *J. Geol. Soc. Lond.* 148, 1019–1036. <https://doi.org/10.1144/gsjgs.148.6.1019>.
- Van Wees, J.-D., Stephenson, R.A., Ziegler, P.A., Bayer, U., McCann, T., Dadlez, R., Gaupp, R., Narkiewicz, M., Bitzer, F., Scheck, M., 2000. On the origin of the southern Permian Basin, Central Europe. *Mar. Pet. Geol.* 17, 43–59. [https://doi.org/10.1016/S0264-8172\(99\)00052-5](https://doi.org/10.1016/S0264-8172(99)00052-5).
- Vaughan, J.R., Hickey, K.A., Barker, S.L.L., 2016. Isotopic, chemical, and textural evidence for pervasive calcite dissolution and precipitation accompanying hydrothermal fluid flow in low-temperature, carbonate-hosted, gold systems. *Econ. Geol.* 111, 1127–1157. <https://doi.org/10.2113/econgeo.111.5.1127>.
- Vazquez, R., Vennemann, T.W., Kesler, S.E., Russell, N., 1998. Carbon and oxygen isotope halos in the host limestone, El Mochito Zn-Pb-(Ag) skarn massive sulfide-oxide deposit, Honduras. *Econ. Geol.* 93, 15–31. <https://doi.org/10.2113/gsecongeo.93.1.15>.
- Wilkinson, M., Crowley, S.F., Marshall, J.D., 1992. Model for the evolution of oxygen isotope ratios in the pore fluids of mudrocks during burial. *Mar. Pet. Geol.* 9, 98–105. [https://doi.org/10.1016/0264-8172\(92\)90007-2](https://doi.org/10.1016/0264-8172(92)90007-2).
- Wilkinson, J.J., Hitzman, M.W., Archibald, S.M., Piercey, S.J., 2015. The Irish Zn-Pb orefield: the view from 2014. *Curr. Perspect. Zinc Depos. Irish Assoc. Econ. Geol. Dublin* 59–72.
- Wilson, M., Neumann, E.-R., Davies, G.R., Timmerman, M.J., Heeremans, M., Larsen, B. T., 2004. Permo-Carboniferous magmatism and rifting in Europe: introduction. *Geol. Soc. London Spec. Publ.* 223, 1–10. <https://doi.org/10.1144/GSL.SP.2004.223.01.01>.
- Xiong, D., Azmy, K., Blamey, N.J.F., 2016. Diagenesis and origin of calcite cement in the Flemish Pass Basin sandstone reservoir (Upper Jurassic): implications for porosity development. *Mar. Pet. Geol.* 70, 93–118. <https://doi.org/10.1016/j.marpetgeo.2015.11.013>.
- Yuan, G., Cao, Y.-C., Gluyas, J., Wang, Y.-Z., Liu, K.-Y., Xi, K.-L., Yang, T., Wang, J., 2019. How important is carbonate dissolution in buried sandstones: evidences from petrography, porosity, experiments, and geochemical calculations. *Pet. Sci.* 16, 729–751. <https://doi.org/10.1007/s12182-019-0344-4>.
- Ziegler, P., 1990. *Geological Atlas of Western and Central Europe*, 2nd ed. Shell International Petroleum MijbV, Geological Society Publishing House, Bath.